RESEARCH ARTICLE

Quantifying gas emissions associated with the 2018 rift eruption of Kīlauea Volcano using ground-based DOAS measurements

Christoph Kern[1] · Allan H. Lerner[2] · Tamar Elias[3] · Patricia A. Nadeau[3] · Lacey Holland[4] · Peter J. Kelly[1] · Cynthia A. Werner[5] · Laura E. Clor[1] · Mike Cappos[3]

Abstract

Starting on 3 May 2018, a series of eruptive fissures opened in Kīlauea Volcano's lower East Rift Zone (LERZ). Over the course of the next 3 months, intense degassing accompanied lava effusion from these fissures. Here, we report on ground-based observations of the gas emissions associated with Kīlauea's 2018 eruption. Visual observations combined with radiative transfer modeling show that ultraviolet light could not efficiently penetrate the gas and aerosol plume in the LERZ, complicating SO_2 measurements by differential optical absorption spectroscopy (DOAS). By applying a statistical method that integrates a radiative transfer model with the DOAS retrievals, we were able to calculate sulfur dioxide (SO_2) emission rates along with estimates of their uncertainty. We find that sustained SO_2 emissions were highest in June and early July, when approximately 200 kt SO_2 were emitted daily. At the 68% confidence interval, we estimate that 7.1–13.6 Mt SO_2 were released from the LERZ during the entire May to September eruptive episode. Scaling our results with in situ measurements of plume composition, we calculate that 11–21 Mt H_2O and 1.5–2.8 Mt CO_2 were also emitted. The gas and aerosol emissions caused hazardous conditions in areas proximal to the active vents, but plume dispersion modeling shows that the eruption also significantly impacted air quality hundreds of kilometers downwind. Combined with petrologic studies of the erupted lavas, our measurements indicate that 1.1–2.3 km^3 dense-rock equivalent of lava were erupted from the LERZ, which is approximately twice the concomitant collapse volume of the volcano's summit.

✉ Christoph Kern
    ckern@usgs.gov

[1] U.S. Geological Survey Cascades Volcano Observatory, Vancouver, WA 98683, USA

[2] University of Oregon, Eugene, OR 97403, USA

[3] U.S. Geological Survey Hawaiian Volcano Observatory, Hilo, HI 96720, USA

[4] University of Hawai'i at Mānoa, Honolulu, HI 96822, USA

[5] U.S. Geological Survey Contractor, New Plymouth, New Zealand

Introduction

The 2018 rift eruption of Kīlauea Volcano is among the most significant events occurring in the past two centuries of activity at the volcano (Patrick et al. this issue). Early in 2018, Kīlauea was erupting in two locations. At the volcano's summit, an active lava lake churning within the Halemaʻumaʻu Crater had appeared in 2008 and was emitting approximately 5000 metric tons per day (t/day) of sulfur dioxide (SO_2) (Elias et al. 2018) and erupting small amounts of fine tephra and spatter (Swanson et al. 2009; Patrick et al. 2018). In the volcano's middle East Rift Zone (MERZ), the Puʻu ʻŌʻō cone and surrounding vents had been erupting since 1983 (Heliker and Mattox 2003). Though SO_2 emissions from Puʻu ʻŌʻō decreased from several thousand t/day to several hundred t/day after the appearance of the summit lava lake (Elias and Sutton 2012), the MERZ remained the primary source of lava flows from Kīlauea, with activity levels varying significantly over the years (Orr et al. 2015).

On 30 April 2018, the floor of Pu'u 'Ō'ō crater suddenly collapsed and geophysical monitoring data indicated that magma drained into a dike extending down into the volcano's lower East Rift Zone (LERZ) (Neal et al. 2019; Anderson et al. 2019). Beginning on 3 May 2018, a series of eruptive fissures opened in the Leilani Estates subdivision of Hawai'i Island's southeastern Puna District. Lava erupted from these fissures, initially with relatively cooler, viscous basalt (approaching basaltic andesite) that had likely been stored within the East Rift Zone (ERZ) for a significant time before being erupted (Gansecki et al. 2019). The lava transitioned to hotter and less viscous basalt throughout the first half of May (Gansecki et al. 2019), and on 19 May, lava flows reached the ocean about 5 km downstream from the fissure locations. Beginning 27–28 May, eruptive activity focused on fissure 8 and remained there for the rest of the eruption, but the location of the ocean entry changed multiple times throughout the eruptive episode as the upstream flow field changed its configuration (Dietterich et al. 2019). The majority of lava effusion ended on 5 August, but some residual activity was observed at fissure 8 until 5 September.

By the time the eruption ended, a total of 24 fissures had opened in the LERZ. Approximately a cubic kilometer of magma had drained from the system (Neal et al. 2019), and lava flows had destroyed more than 700 structures. The volume of magma removed from the volcano's plumbing system led to large-scale caldera collapse at the summit. The lava lake in the Halema'uma'u Crater drained out of sight by 10 May, and the entire caldera began deflating. During the course of the eruption, some areas of the summit caldera had dropped by more than 500 m (Neal et al. 2019) and faulting on the caldera boundaries caused large blocks to slump inward. The combination of this faulting and slumping eventually damaged the historic Hawaiian Volcano Observatory (HVO) building such that it had to be abandoned.

SO_2 continued to be emitted at the summit and MERZ throughout the eruption, but as fissures opened in the LERZ, it quickly became the dominant source of degassing activity. Lava and gases emitted from the fissures posed an immediate and significant hazard to residents and visitors. While the potential paths of future lava flows were relatively straightforward to forecast based on lines of steepest descent, the hazard from inhalation of volcanic gases, in particular SO_2, was dependent on source location, gas emission rate, and wind conditions, all of which were varying throughout the eruptive episode. Depending on wind speed and direction, the short-term exposure limit of 5 parts per million by volume (ppmv) averaged over 8 h as recommended by the Occupational Safety and Health Administration (OSHA) of the United States Department of Labor (NIOSH 1978) was often significantly exceeded at locations many kilometers downwind of the active fissure 8 vent. The local flora was also severely impacted, with large-scale vegetation-kill zones quickly appearing in areas exposed to high gas concentrations.

As soon as the rift eruption began, the U.S. Geological Survey's HVO began quantifying SO_2 emission rates by making vehicle-based differential optical absorption spectroscopy (mobile DOAS) measurements of the emitted gas plumes (USGS 2018). Information from these measurements was provided to partner agencies responsible for public safety in order to assess local and regional gas-related hazards. At the same time, these measurements allowed for tracking the progression of the rift eruption and provided timely information for use in forecasting air quality.

By mid-May, as lava effusion and degassing rates increased substantially, it became clear that the standard DOAS analysis methods used for determining volcanic SO_2 emission rates from mobile DOAS measurements (Galle et al. 2002; Kantzas and McGonigle 2008) were no longer applicable. The emitted plumes had become so optically opaque due to high concentrations of aerosols along the mobile DOAS measurement route that solar UV radiation was no longer able to fully penetrate the plume on its way to the instrument on the ground (Kern et al. 2010, 2012). This circumstance had to be considered when analyzing the collected DOAS data.

In this article, our best estimates of gas emission rates and cumulative gas emissions associated with Kīlauea's 2018 LERZ eruption are presented. To begin, we provide a description of the optical properties of the gas plumes encountered while making mobile DOAS measurements. During the periods of highest emissions in June and July, some key observations allowed inferences about the radiative transfer occurring in and around the plumes. Results from a radiative transfer model initialized to simulate the encountered conditions provided additional insights into effective light paths and implications for the sensitivity of the measurements. Based on these findings, a new retrieval method is outlined. Using a statistical inversion technique, best estimates for SO_2 emission rates were derived along with associated uncertainties, even during periods of intense volcanic degassing and highly opaque plumes. Finally, the results of the analyses are presented, and the magnitude of gas emissions is placed into the context of other recent eruptions occurring at volcanoes around the world. The implications of our observations on the conceptual model of Kīlauea's 2018 rift eruption are examined, and the impacts of the large-scale gas emissions on the surrounding environment are discussed.

Optical properties of gas plumes in the LERZ

HVO's efforts to track sulfur dioxide emissions during the LERZ eruption were primarily focused on performing mobile DOAS driving traverses beneath the gas plume. These traverses were made in conditions during which trade winds transported the emitted gases to the southwest, where the

plume was intersected either on State Highway 130 between Pāhoa and Kalapana or on Kama'ili Road between State Highway 130 and Opihikao (Fig. 1). Depending on which fissures were active and the exact wind direction, the gas plume was typically traversed 3–6 km from the point(s) of emission. The road network did not allow for traverses to be made at greater distances under typical wind conditions.

By the beginning of June, SO_2 emission rates likely exceeded 100 metric kilotons per day (kt/day). Thus, we encountered plumes with extreme SO_2 concentrations (> 1000 ppmv) at relatively short distances from the emission source (Kelly et al. this issue). In these extreme circumstances, we were able to observe several optical scattering and absorption effects that, while typical for volcanic plumes as a whole, are usually less pronounced and therefore more difficult to identify. In this section, we first present visual observations of the plume and then move on to more quantitative modeling of the plume's optical properties.

Visual observations of plume optical properties

Gases and aerosols emitted from active fissures in Kīlauea's LERZ were injected into the high-humidity atmospheric environment of Hawai'i Island's windward side. During typical trade-wind conditions, northeasterly winds blow humid air masses onshore where they are subject to orographic lifting against the east flanks of the volcanoes (Giambelluca et al. 2013). Convective cloud formation is common, as condensation releases latent heat and provides buoyancy. Throughout the course of the 2018 rift eruption, but particularly in June and July when activity was at its peak, convective clouds and rain showers systematically formed over and directly downwind of the active fissures, with cloud tops commonly reaching many kilometers in altitude. These clouds, called pyrocumulus or flammagenitus clouds, can form over wildfires or active volcanoes when significant amounts of water vapor, latent and sensible heat, and aerosols are released
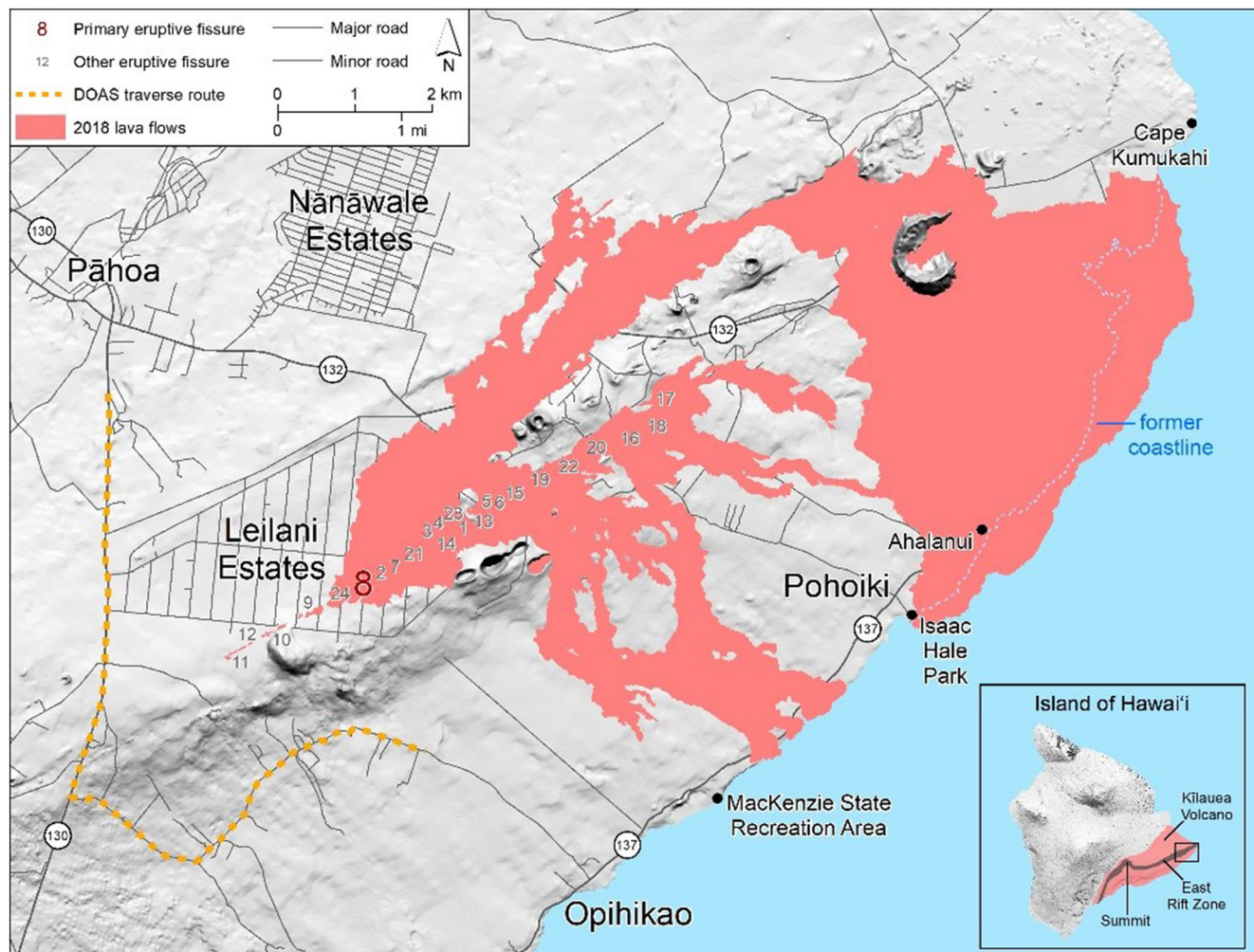

Fig. 1 Map showing the extent of LERZ lava flows as lava effusion was coming to an end in early August 2018. The most prodigious source of lava and gas emissions during the eruption, fissure 8, is highlighted. Routes where vehicle-based DOAS traverses crossed beneath the plume under trade-wind conditions are marked in orange

into the atmosphere (Gatebe et al. 2012; Poulidis et al. 2016; Barahona et al. 2019). Depending on wind direction, the water plume rising from the lava flow's ocean entry also likely contributed to the pyrocumulus systems forming over the LERZ.

We restricted our mobile DOAS traverse measurements to times during which there was no heavy rainfall downwind of the fissures. Still, the gas and aerosol plume mostly took the appearance of a dense, dark gray meteorological cloud. Sometimes, however, scattering of sunlight on small sulfate aerosols in the plume would give it slight blue or orange hues (Fig. 2), depending on lighting conditions.

Most volcanogenic sulfate aerosols form as SO_2 reacts with atmospheric oxidants in chemically evolving volcanic plumes (von Glasow et al. 2009). However, measurements performed at vigorously degassing, high-temperature volcanic vents have shown sulfate aerosols are already present directly at the point of emission (Allen et al. 2002). These particles are either emitted as solids from the vent or are rapidly formed in high-temperature gas-phase reactions occurring at the vent itself, and particle concentrations in the near-vent area can be significant. Aerosols grow in size over time as they provide nuclei for condensation in water clouds or coagulate with other particles, but close to the vent, most particles are in nucleation or accumulation modes and have effective radii of less than 250 nm (Mather et al. 2003; Sawyer et al. 2011; Roberts et al. 2018; Ilyinskaya et al. 2020).

A particle's size governs its interaction with solar radiation. Scattering of light on aerosol particles is described by Mie theory (Mie 1908). The scattering efficiency is inversely related to the mean particle radius, but for particles larger than the radiation wavelength (λ), scattering occurs with only a weak wavelength dependency. For example, meteorological water clouds contain water droplets larger than the 400–800 nm wavelengths of visible light. Thus, all visible light is scattered approximately equally, and clouds appear in various shades of white or gray but generally do not exhibit a hue unless illuminated by colored light at sunrise or sunset. On the other hand, scattering on particles with radii comparable to, or slightly smaller than, visible wavelengths can exhibit a much stronger wavelength dependency, with short wavelengths being scattered more efficiently than longer ones. These and other atmospheric scattering processes are described in detail by Platt and Stutz (2008) and references therein.

Visual observations of the plumes emitted from active fissures in the LERZ detected distinctive plume colors, consistent with the presence of small sulfate aerosols. If, for example, the plume was viewed with the sun behind the observer, it often had a slightly blue appearance (Fig. 2a). In this situation, sulfate aerosol particles scatter shorter-wavelength blue light back at the observer more efficiently than the longer-wavelength red colors (Ammann and Burtscher 1993; USGS 2018). In other situations when the plume was back lit either
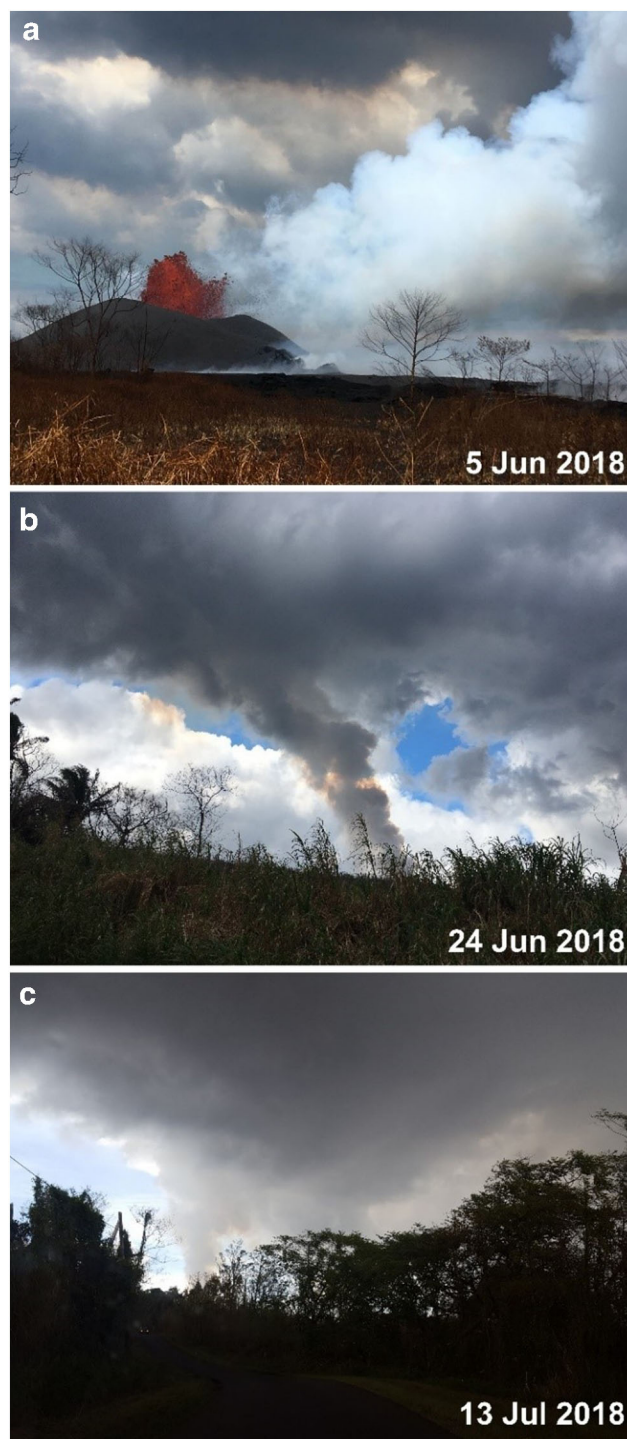

Fig. 2 Photographs of the gas and aerosol plume emitting from fissure 8 in Kīlauea's lower East Rift Zone. **a** With the sun located behind the observer taking this photograph, light scattered back to the camera on small sulfate aerosols causes the plume to appear blue. The spatter cone is approximately 35 m high in this image. **b** In this photograph, the plume is back-lit and the same scattering processes remove blue light and cause the plume to appear orange. This plume is within a few hundred meters of the ground. **c** Conditions beneath the plume were often so dark that vehicles needed to use headlights. According to our measurements, the plume in this image was centered approximately 700 m above ground level. Plumes commonly remained within a few hundred meters of the ground while drifting to the measurement location 3–6 km downwind

by the sun or by bright white clouds behind it, it would often appear orange or brown (Fig. 2b) (USGS 2018). Here, blue light entering the back of the plume was preferentially scattered away from the observer. Longer-wavelength orange and red light was more likely to pass through and reach the observer, thus making the plume appear orange.

Red discoloration effects from scattering of light on sulfate aerosols were observed throughout the eruption, but they were often limited to the plume edges. In the plume center, light was generally not able to pass through the plume, regardless of wavelength. Thus, plumes would appear visibly dark in their core. When traversing beneath such plumes, our DOAS instruments recorded a considerable drop in incident radiation across the entire 300–420 nm measured spectral window.

The aerosol optical depth (AOD) is a measure of light attenuation due to interaction with aerosols. For the moment ignoring absorption of light by gases, the AOD is defined as the exponent in the Beer-Lambert-Bouguer law (Bouguer 1729; Platt and Stutz 2008) which describes attenuation of a narrow beam of light entering an aerosol cloud.

$$I = I_0 \cdot e^{-\text{AOD}} \qquad (1)$$

where I_0 is the initial light intensity and I is the intensity of the light beam after passing through the cloud. Scattering is usually the dominant attenuation process, but in this form, the AOD encompasses attenuation by both scattering and aerosol absorption. When the AOD is used to describe the background atmosphere, I_0 corresponds to the light beam intensity at the top of the atmosphere and I describes the intensity that reaches the Earth's surface. The atmospheric AOD is closely related to visibility, with typical values ranging from 0.01 for an extremely clean atmosphere to about 0.8 for severe haze (Zhang et al. 2020). Here, we will apply the AOD to describe the volcanic plume. In this case, I_0 is the light beam intensity at the top of the plume and I is the intensity that remains after passing through the plume. As shown in the next section, the AODs associated with the extremely opaque volcanic plumes we encountered were much greater than even the haziest atmospheric conditions.

The single-scatter albedo (SSA) gives the probability that a photon interacting with an aerosol particle is scattered rather than absorbed (Platt and Stutz 2008).

$$\text{SSA} = \frac{\varepsilon_s}{\varepsilon_s + \varepsilon_a} \qquad (2)$$

where ε_s is the aerosol-scattering coefficient and ε_a is the absorption coefficient. An SSA of 1 therefore indicates a purely scattering aerosol, while values smaller than 1 indicate a finite probability of absorption. Mixed volcanic aerosols containing sulfate particles and low to moderate abundances of volcanic ash will typically exhibit SSAs in the range of 0.75 to 0.95 in UV wavelengths (Krotkov et al. 1997).

Based on our visual observations of the dark plumes emitted from active fissures in the LERZ (Fig. 2c), these clearly exhibited very high optical depths. As we will show more quantitatively in the next section, it is not valid to assume that light measured with our DOAS spectrometer had passed through the plume along a straight, vertical line. Instead, SO_2 column densities measured by the DOAS should be interpreted as columns along a complex light path about which little is known. This complicates the process of determining SO_2 emission rates, as measured SO_2 column densities cannot simply be integrated across a plume traverse in order to determine the plume's cross-sectional SO_2 burden, as is commonly done (Galle et al. 2002). Instead, the measured column densities must first be converted to representative vertical column densities based on estimates of the effective light path for each measurement.

Modeling plume optical properties

In order to gain further insight into the path length distribution of light as it passes through these dense volcanic plumes, we used a radiative transfer model to simulate the conditions of our measurements. The simulations were performed using the three-dimensional atmospheric radiative transfer model McArtim (Deutschmann et al. 2011). This model simulates the propagation of monochromatic light through a model atmosphere and includes Rayleigh scattering on air molecules, scattering on and absorption by aerosols, as well as trace gas absorption by any number of absorbing gas species defined in the atmosphere.

In previous work, McArtim has been used successfully to evaluate the effect of light scattering on DOAS measurements for a number of common volcanic observation scenarios (Kern et al. 2010). In an approach called simulated radiative transfer DOAS (SRT-DOAS), the model was coupled with DOAS analyses to derive corrected vertical columns and SO_2 emission rates for measurements performed in well-defined measurement geometries (Kern et al. 2012). The SRT-DOAS approach relies on generating N-dimensional spectral lookup tables, where N is the number of variable physical parameters influencing the radiative transfer of the measurements, and then comparing these simulated spectra with the measured spectra.

With the SRT-DOAS approach in mind, we used McArtim to explore the influence of various parameters on our measurements. Quantifying the plume conditions required to generate the encountered visually dark plumes was a logical starting point. In this context, we define the plume *darkening* as the ratio of downwelling radiance incident below the plume (I_p) to the downwelling radiance away from the plume (I_0). Both aerosols and absorbing gases will lead to light attenuation and influence the darkening. To separate the two effects, we focus on a single wavelength (367 nm) which is accessible to

our spectral measurements but at which SO_2 absorption is negligible (it is between weak SO_2 absorption bands), so light attenuation at this wavelength can be considered solely caused by aerosol attenuation.

Note that the darkening ratio I_p/I_0 is closely related to the plume's AOD (Eq. (1)), but the three-dimensional radiative transfer model allows us to move away from the narrow-beam approximation and consider a realistic scenario in which scattered solar radiation enters the plume from all directions and may also pass around the plume entirely before being recorded by the DOAS spectrometer. By running model simulations for various plume conditions, we can examine the relationship between I_p/I_0 and plume AOD. Figure 3 shows that as aerosols are introduced into a volcanic plume and the AOD increases, the plume initially becomes brighter. In this regime, the plume aerosols increase the scattering of sunlight towards the instrument on the ground, thus increasing the downwelling radiance I_p above background levels.

Only after the AOD increases above a certain threshold (5–10 depending on the aerosol SSA) does the plume begin to appear darker than the background. In order to reproduce I_p/I_0 ratios of < 0.1 as were commonly measured when passing under the densest gas clouds of the eruption, aerosol optical depths exceeding 10 and possibly as high as 40 are required. The results also show that the aerosol SSA has significant impact on I_p/I_0, especially at high AODs where light entering the plume commonly has multiple interactions with aerosol particles.

After ascertaining the range of realistic plume AODs based on our observations of plume darkening, we examined the effective leng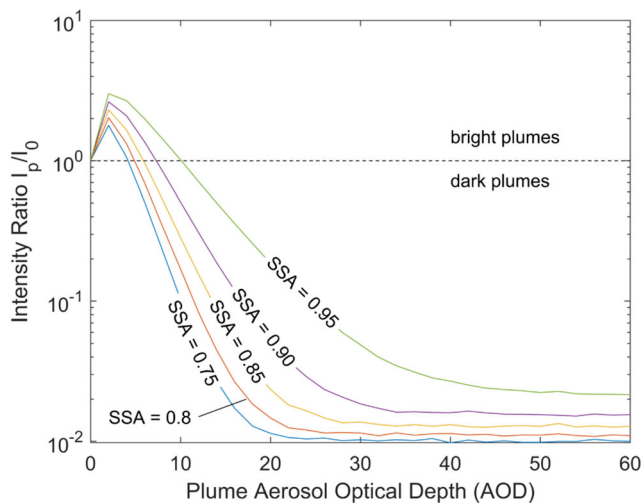th of light paths in these conditions. As is common in the remote sensing literature (Platt and Stutz 2008), we define the air mass factor (AMF) as the ratio of the effective light path length (L) within the plume to the plume's vertical extent (V).

$$\text{AMF} = \frac{L}{V} \qquad (3)$$

According to this definition, an AMF larger than 1 indicates path length extension while an AMF smaller than 1 indicates that the effective path along which the measurement of SO_2 column density is made is shorter than the straight, vertical line through the plume. Such shorter paths are possible if a significant portion of the measured radiation enters the plume from the side or from below, or misses it entirely.

Our simulations showed that both extension and reduction of the effective light path length are possible in our measurement conditions (Fig. 4). As aerosols are added to the plume and the AOD increases, effective path lengths initially become longer because light is scattered multiple times before reaching the instrument. However, at AODs between 10 and 40, which correspond to the dark plumes we often encountered in our measurements, the AMF drops below 1 because light can no longer penetrate the plume center and the radiation that does reach the ground has often only passed through the outer layers of the plume before being scattered towards the instrument. Also, the results again highlight the significant impact that the aerosol SSA has on the light path distribution. Scattering aerosols increase the probability of longer light path

Fig. 3 Radiative transfer model results showing the ratio of downwelling radiance at 367 nm under the plume (I_p) to that away from the plume (I_0). For this simulation, the plume was centered 900 m above the instrument. Measurements of I_p/I_0 were commonly < 0.1 when passing under thick gas clouds from fissures in the LERZ. Depending on the SSA of the plume aerosol, this implies plume optical depths greater than 10 and possibly as high as 40 or more
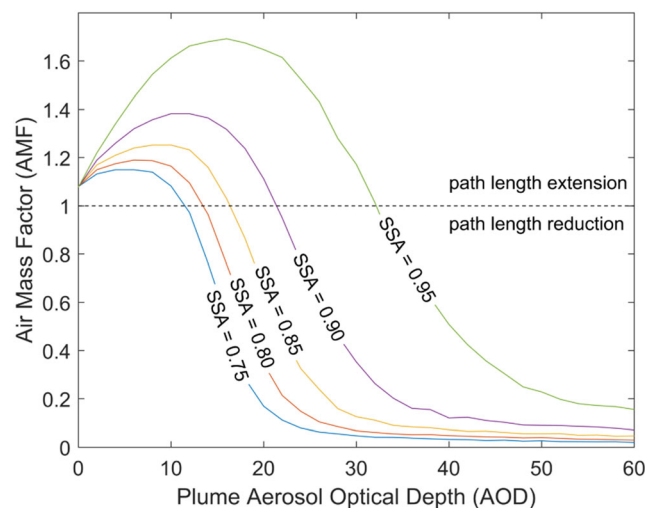

Fig. 4 Results from radiative transfer model simulations showing the effect of an increasing plume aerosol optical depth (AOD) on the effective light path length at 367 nm, again assuming a plume centered 900 m above the instrument. As the AOD increases, light paths initially become longer (AMF > 1) due to multiple scattering within the plume. For very high optical depths > 10, however, effective path lengths decrease as aerosol attenuation removes light passing through the plume center, and the relative contribution of radiation passing only through the plume edges or missing it entirely increases

lengths, while more absorbing aerosols significantly decrease the expected AMF for a given AOD.

Further exploring the factors controlling radiative transfer in our measurements, we found that the height of the plume above our instrument also plays an important role. In Fig. 5, the AMF is plotted as a function of the plume altitude. For an intermediate SSA of 0.875, we again find that the AMF initially increases with increasing AOD (compare to Fig. 4), indicating initially longer path lengths of light passing through the plume. This increase in path length by multiple scattering within the plume as aerosols are added occurs regardless of plume height. However, as the AOD increases to values greater than 10 at which light attenuation becomes significant, the simulated drop in AMF depends on plume height. Light is more likely to enter the spectrometer's field of view without having passed through the plume if the plume is high and far from the instrument than it is for low, close plumes. This is equivalent to the so-called "light dilution" effect (Mori et al. 2006; Kern et al. 2010; Campion et al. 2014), which is more pronounced for distant plumes.

In conclusion, our radiative transfer simulations showed that the plume AOD, the aerosol SSA, and the plume height all influence the light path distribution along which our measurements were made. Unfortunately, we have no independent means of measuring the predominant aerosol SSA encountered during our measurements and are instead forced to allow for a range of possible values. Similarly, we do not have reliable plume height information for most of the collected data. Towards the end of the eruption, a dual-beam mobile DOAS
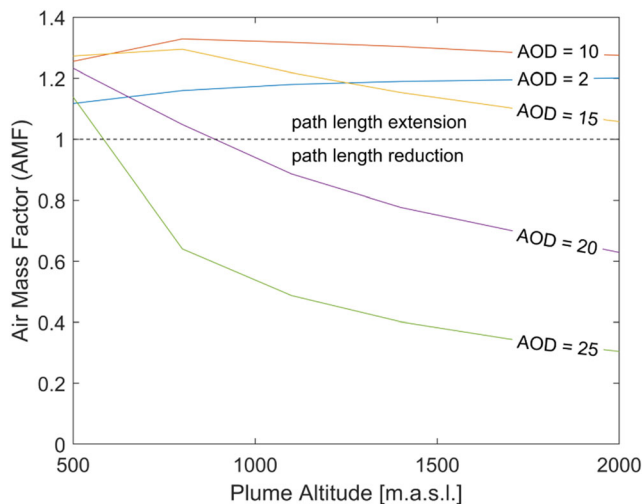

Fig. 5 Results from radiative transfer model runs examining the sensitivity of our ground-based DOAS measurements on plume height. Assuming an aerosol SSA of 0.875, we find that the light path length initially increases with increasing AOD (compare Fig. 4). This effect occurs regardless of the plume altitude. As AODs increase beyond 10 and the plume becomes dark, the effective light path decreases in length. This shortening is more pronounced for high plumes, as light can pass around these more easily and still enter the spectrometer on the ground than for low-level gas clouds

instrument was implemented (McGonigle et al. 2005; Johansson et al. 2009). This allowed us to derive plume heights for a subset of the dataset, and we found that the altitude of the plume center varied from day to day between about 600 and 1600 m above sea level.

While theoretically possible, taking variations of plume height and aerosol SSA into account in addition to the plume AOD and the actual abundance of SO_2 in an SRT-DOAS analysis would require a 4-dimensional spectral lookup table which we found prohibitively computationally expensive to generate. It is also unclear whether the information content of our spectral measurements in the 300–420 nm wavelength range is sufficient to retrieve all four variable parameters. We therefore adopted a different approach to integrate measurements with model simulations while accounting for the realistic consequences of uncertainties in our understanding of the measurement conditions.

Methods: determining SO_2 vertical column densities and emission rates from ground-based DOAS measurements

After simulations showed that our DOAS measurements were being influenced by complex radiative transfer in the extremely thick gas and aerosol plumes emitted from fissures in the LERZ, we developed a statistical method for taking these effects into account. In the sections below, we describe each step of the methods used to develop our best estimate of SO_2 emissions associated with the Kīlauea's 2018 fissure eruption.

Retrieving SO_2 slant column densities from the measured spectra

To characterize SO_2 emission rates from Kīlauea's LERZ, an upward-looking mobile DOAS spectrometer (Ocean Optics SD2000) was used to record moderate-resolution (0.7-nm) spectra of scattered solar UV radiation in the 300–420 nm wavelength range while being driven in traverses beneath the gas plume (Galle et al. 2002). Spectra were collected using a 1-s integration time, with the exposure time of individual exposures being adjusted to account for changes in light intensity. Whenever exposure times were sufficiently short, multiple exposures were co-added within a given 1-s interval.

Initially, standard DOAS procedures were used to retrieve the SO_2 vertical column density between 310 and 340 nm for each collected spectrum (Galle et al. 2002, 2010; Platt and Stutz 2008). However, we soon realized that our obtained SO_2 column densities were dependent on the wavelength range chosen for the retrieval. Adjusting the retrieval window towards longer wavelengths resulted in an increase in SO_2 column densities. This effect has been observed elsewhere (Mori et al. 2006; Kern et al. 2010, 2012; Bobrowski et al.

2010; de Moor et al. 2016; Fickel and Delgado Granados 2017) and is a result of gases and aerosols in optically thick plumes influencing the light path distribution along which the measurements are made. In such situations, one can no longer assume that the DOAS measurements are integrating along a straight, vertical path through the plume. Instead, the retrieved column densities should be interpreted as the integral of the SO_2 concentration c_{SO_2} along an unknown effective light path L (Kern et al. 2010, 2012). Consistent with the existing DOAS literature (Platt and Stutz 2008), we refer to them as slant column densities (SCDs).

$$\mathrm{SCD}(\lambda) = \int_{L(\lambda)} c_{SO_2} dl \qquad (4)$$

Many effects that govern radiative transfer in and around opaque volcanic plumes are dependent on wavelength (Kern et al. 2010), so it is not surprising that L and therefore the SCD also depend on the wavelength λ of the measurement. One of the main causes for this effect stems from the wavelength-dependent SO_2 absorption cross section (Vandaele et al. 2009). Simply moving the DOAS fit window from 310–340 to 319–340 nm reduces the maximum considered SO_2 absorption cross section by about a factor of 6, thus moving to a spectral range in which significantly more light can pass through the gas plume at the cost of a reduced measurement sensitivity to SO_2.

In extreme cases, certain areas of the UV spectrum can become almost entirely absorbed by SO_2. A plume containing 100 ppmv of SO_2 over a plume thickness of 100 m would absorb 99.99% of incident radiation at 310.7 nm and 75% at 319.6 nm, while only absorbing about 2% on the much weaker SO_2 absorption band at 370.2 nm (Vandaele et al. 2009). The practical consequence of strong absorption at short wavelengths is that measurements in this range will no longer contain information on the plume core. This is because light paths passing only through the outer, less-concentrated plume or missing the plume entirely become much more probable than the straight path through the plume center. Thus, most of the light received by the instrument has not passed through the plume core and does not carry any information about it.

In cases of high SO_2 burdens, it is therefore always preferable to move to spectral evaluation ranges where trace gas absorption is weak, i.e., where less than about 10% of incident light is absorbed. We used three different evaluation ranges to process our DOAS spectra. First, a DOAS retrieval was run in the 345–390-nm-wavelength region where SO_2 absorption is 2 to 3 orders of magnitude weaker than in the standard 310–340-nm region. This represents only a slight modification of the 360–390 nm range suggested by Bobrowski et al. (2010) which allowed us to evaluate a few additional SO_2 absorption bands.

Each measured spectrum was first corrected for the detector's electronic offset and dark current, then the logarithm was applied. Implemented in the DOASIS software (Kraus 2004), a Levenberg-Marquardt least-squares fit was then used to fit the logarithm of a plume-free spectrum to the measurement, allowing for a slight shift (< 0.2 nm) and squeeze (< 5%) of the spectrum to compensate for effects induced by varying temperatures of the spectrometer optical bench. At the same time, the absorption cross sections of SO_2 (Vandaele et al. 2009), O_3 (Bogumil et al. 2003), O_4 (Hermans 2010), and NO_2 (Bogumil et al. 2003) were included in the fit to describe differences in the measurement and clear-sky spectra, as prescribed in the standard DOAS model (Platt and Stutz 2008). Also included in the fit, a Ring correction spectrum (Grainger and Ring 1962) was used to account for the variable contribution of rotational Raman scattering to the measured downwelling radiance, and a third-order polynomial was used to account for broadband absorption and scattering processes.

Despite its relatively weak absorption cross section in the 345–390 nm range, SO_2 could be clearly identified and quantified when traversing beneath the plume core. Figure 6 shows an example analysis, with an SCD of 2.4×10^{20} being retrieved from the best fit of the SO_2 absorption cross section to the measured differential optical depth. This corresponds to approximately 100,000 parts per million × meters (ppmm) of SO_2. Values of this order of magnitude were common during the LERZ eruption. Though the DOAS method cannot resolve the distribution of SO_2 along the effective light path of the measurements, such a column density could, for example, be obtained if an SO_2 mixing ratio of 200 ppmv was sustained along a path of 500 m.

The fit range 345–390 nm was well suited for the analysis of most of the collected data, but particularly at the plume edges where gas concentrations were lower, the sensitivity of the retrieval in this region was insufficient. Using the fit residual to determine the standard error of each retrieved SO_2 SCD (Stutz and Platt 1996), cases in which the SCD was less than twice the uncertainty of the measurement were flagged. These spectra were then re-analyzed in the 319–340 nm wavelength range. Here, the cross sections of NO_2 and O_4 were not considered as they do not have significant absorption features in this region. Only during the very last measurements of waning degassing from the LERZ activity after 5 August 2018 did the sensitivity of the retrieval need to be increased further, so the fit range was adjusted to the 310–340-nm window or, if illumination conditions allowed, to 305–340 nm.

A statistical method to convert slant columns to vertical columns

After SO_2 SCDs were retrieved for all collected spectra, the next step in determining emission rates was to convert the SCDs to vertical column densities (VCDs). Though the choice of spectral fit region should avoid strong SO_2 absorption in the plume core which can promote signal dilution, moving towards weak absorption does not entirely eliminate dilution caused by light entering the
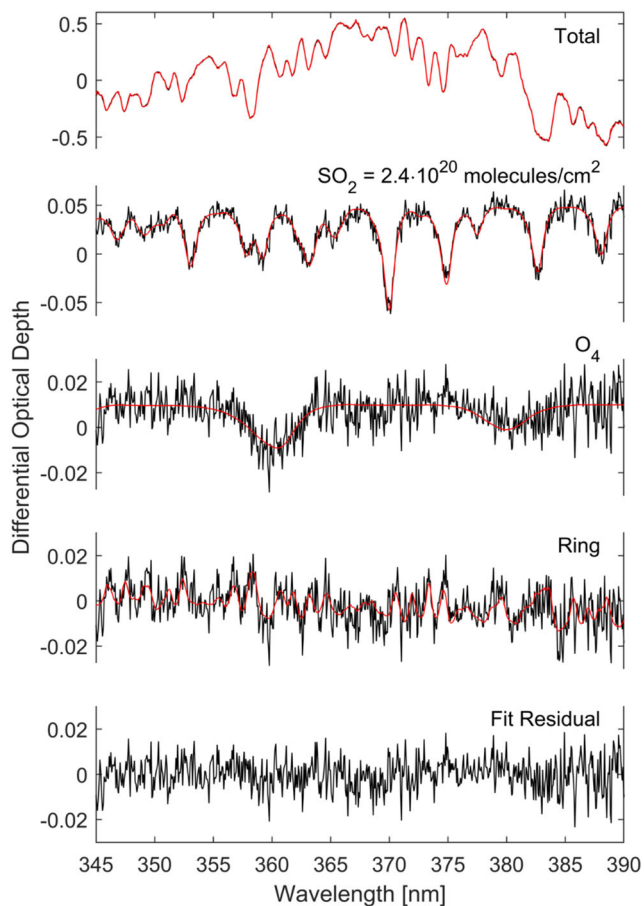
Fig. 6 Example DOAS spectral retrieval performed in the 345 to 390 nm wavelength range. The spectrum analyzed in this example was recorded at 01:45 UTC on 14 June 2018 while traversing the gas plume emitted by fissure 8 in the LERZ. The SO_2 absorption lines were clearly identified, and a slant column density (SCD) of 2.4×10^{20} molecules/cm^2 was determined from the fit. Besides SO_2 absorption, the absorption of light by O_4 and the Ring effect could clearly be identified. Not shown are the absorption cross sections of O_3 and NO_2, as absorption by these species was negligible in this fit

spectrometer's field of view without passing through the plume. Significant light dilution would cause measured SO_2 SCDs smaller than the VCD. On the other hand, multiple scattering within the plume can lead to an extension of the effective light path, thus leading to measured SCDs higher than the VCD (Kern et al. 2010, 2012).

Realizing the potential significance of light dilution and multiple scattering in the measurements of extremely dense volcanic plumes, we developed a statistical framework to take them into account and retrieve realistic VCDs. Largely following recommendations by Mosegaard and Tarantola (1995), a Markov chain Monte Carlo (MCMC) algorithm was implemented to retrieve probability distributions of the physical state of the overhead volcanic plume based on our spectral measurements combined with radiative transfer simulations of possible measurement conditions. In this section, we describe this statistical method.

The measured spectra are the result of complex interactions of UV radiation with the atmosphere and overhead volcanic plume. For each spectrum, we can retrieve two derived data products: the darkening ratio I_p/I_0 and the SO_2 SCD. I_p/I_0 is derived by simply calculating the ratio of light intensities measured at 367 nm, and the SO_2 SCD is retrieved using the DOAS analysis described in the previous section. Because I_p/I_0 is determined at 367 nm where SO_2 absorption is negligible, this ratio is independent of the overhead SO_2 burden and depends only on the optical characteristics and spatial distribution of aerosols in the plume. On the other hand, the SO_2 SCD depends primarily on the SO_2 abundance in the plume but is also affected by the aerosol properties as these govern the effective light path along which the SCD is measured. Besides these two derived parameters, we were able to constrain the plume height in measurements collected between 10 July and 4 August using a dual-beam DOAS system. Together, these three parameters, along with their uncertainties, make up the information content of each of our observations.

The goal of our measurements is to derive the physical state x' of the volcanic plume. For the purpose of our data analysis, it is useful to describe the plume using parameters which can be considered in our radiative transfer model McArtim: the plume height, the SO_2 VCD, the AOD, and the aerosol SSA. To reduce complexity, we are also forced to make several assumptions which, though not entirely realistic, are not expected to influence the retrieved results significantly: (1) We assume the plume to extend infinitely in one spatial dimension, sliced perpendicularly by our measurements; (2) the plume cross section is approximated by a rectangle, with the plume horizontal width equaling twice its height above the ground (roughly consistent with our dual-beam observations) and a constant plume thickness of 500 m; (3) the gas and aerosol distributions within the plume are considered constant and homogenous, as no information on the actual spatial distributions is known from our measurements; and (4) the sun is located at a 30-degree zenith angle with an azimuth neither parallel nor perpendicular to the plume.

With this framework in place, an MCMC algorithm was run on every measured spectrum to determine a best estimate of the associated SO_2 VCD. The algorithm involves five steps which are run in sequence and repeated thousands of times until stable output probability distributions are obtained (Fig. 7).

In the *first step*, some physical state x' is assumed. The first time the algorithm is iterated, this state can either be chosen entirely at random, or some a priori estimate of the actual physical state can be used. The radiative transfer model is initialized with this assumed physical state, and in the *second step*, the model is used to simulate an observation of this state. Specifically, McArtim simulates the SO_2 SCD and the darkening ratio I_p/I_0 for a given SO_2 VCD, AOD, aerosol SSA, and plume height.

Fig. 7 Flow diagram of the MCMC algorithm used to derive information on the physical state of the overhead volcanic plume. This process was repeated thousands of times for each measured spectrum, thus generating a histogram of physical states that are consistent with each measurement of SO_2 SCD and I_p/I_0
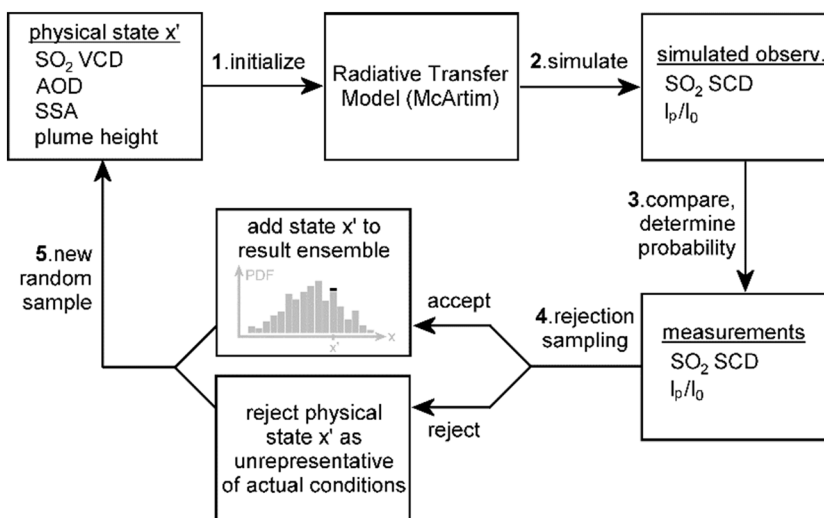
In the *third step*, the simulated SO_2 SCD and I_p/I_0 are compared to the values retrieved from the current measured spectrum. The measured parameters are assumed to be normally distributed around their retrieved values, and the retrieved uncertainties are assumed to be standard symmetrical errors. Thus, each measurement result is associated with a probability density function (observation PDF). A simulated measurement result can therefore easily be assigned a relative probability based on where it falls on the PDF of the actual observations.

In the *fourth step*, we use a simple rejection sampling approach to either accept or reject the physical state x' that formed the basis of our simulation. We normalize the observation PDF such that its peak value is unity. We then draw a random number between 0 and 1 and compare this number to the value of the observation PDF evaluated at the point of the simulated observation. If the value of our random number falls within the observation PDF, we accept the simulation and the physical state x' on which it was based. In this case, we add the parameter values describing x' to an ensemble of parameters describing realistic conditions. If, on the other hand, the value of our random number lies outside of the observation PDF, we reject the physical state x' as unrealistic because the simulations showed that this state does not lead to observations consistent with our measurement results.

In the *fifth and final step*, a new, different physical state x' is selected, and the entire process is repeated. The new sample is not chosen completely at random but instead follows the so-called "Metropolis-Hastings algorithm" (Metropolis et al. 1953; Hastings 1970). Here, a candidate for the next sample is chosen based on a stepwise modification of the last accepted previous state. If the current iteration led to a simulated observation with an acceptable probability when compared to the measurement (see step 4), this new state is used as a basis from which to *jump* to a new, probably nearby state. If, on the other hand, the current iteration was rejected as inconsistent with the

measurement, the previous state is kept as the basis from which to jump to the next sample state. This sampling method, in which the next sample state is dependent on the probability of the current sample, is equivalent to a so-called "Markov chain" (Markov 1906) and gives the algorithm its name. Use of this method decreases the chances of sampling states that will be rejected in step 4 of the algorithm, thus increasing its computational efficiency over naive random sampling.

As the algorithm is iterated, the ensemble of realistic physical states that are consistent with the measurements grows. At any time during the process, histograms of these realistic conditions can be generated and displayed. These histograms not only give the most likely physical state of the volcanic plume given the measurement results but also show the probabilities of other possible states, thus providing us with probability distributions for SO_2 VCD and plume AOD.

Optimization of the MCMC algorithm

One drawback of the MCMC approach is that it is associated with a significant computational cost. After studying the output distributions as a function of the number of iterations, we found that at least 20,000 iterations of the code were required to stabilize the output and ensure convergence to the desired, sufficiently smooth distribution. In order to save time, two additional steps were taken to optimize performance.

The main computational cost of the algorithm as shown in Fig. 7 stems from running the radiative transfer model in each iteration. Therefore, we generated pre-computed lookup tables covering the reasonable parameter space of possible plume conditions and simply performed a lookup operation on these tables during the MCMC runs (see Online Resource 1).

Secondly, we used informed a priori estimates when initializing the aerosol SSA and plume heights in step 1 of the algorithm. Since the information content of our measurements did not further inform these two parameters, they were then

omitted from the rejection sampling scheme, thus reducing the number of rejected simulations and improving performance. For the SSA, we assumed a normal distribution centered at 0.875 with a standard deviation of 0.03 that covers the full range of plausible values (see, for example, Krotkov et al. 1997). For the plume height, we used information from the dual-beam DOAS measurements when available, adding a standard deviation of ± 100 m to account for measurement errors. When no plume height information was available, we sampled from a uniform distribution, assigning equal probability to all plume heights between the minimum (600 m) and the maximum (1600 m) heights above sea level obtained during our dual-beam measurements in July and August.

Even with the above-described optimizations, the computational cost of analyzing all our data using the MCMC method was significant. However, one great advantage of Monte Carlo methods is that their performance can be greatly improved using parallel computing techniques. After developing a parallel implementation of our algorithm, we were able to process approximately one spectrum every 2 s on a modern desktop computer with four physical processor cores.

Example VCDs and AODs obtained from the MCMC algorithm

Figure 8 shows examples of output histograms for both the SO_2 VCD (Fig. 8a) and the AOD (Fig. 8b). These histograms were generated from an ensemble of results obtained after applying our MCMC algorithm to the spectrum shown in Fig. 6. The histograms show that the most likely value of the SO_2 VCD (mode of the distribution) at this measurement location was 2.3×10^{20} molecules/cm^2 which is remarkably similar to the SCD derived from the 345–390-nm DOAS retrieval. This indicates that the effective light path of the measurement at 345–390 nm may have been reasonably similar in length as the straight, vertical path through the plume.

However, note also that the calculated distribution is asymmetrical. SO_2 VCDs greater than the mode appear to be far more likely than values smaller than the mode. The broad shoulder of the distribution towards higher VCDs indicates that, instead of taking a straight, vertical path through the plume, there is a significant probability that light may instead have passed around the plume core on its way to the instrument. In this case, some of the measured light would miss the plume entirely, the effective path length within the plume would be shorter than its vertical extent, and the actual SO_2 VCD would be greater than the DOAS-derived SCD. On the other hand, the sharp lower edge of the histogram indicates that it is unlikely multiple scattering on plume aerosols caused long light paths within the plume, thereby causing the DOAS-derived SCD to exceed the VCD. This example asymmetrical distribution is broadly representative of most histograms
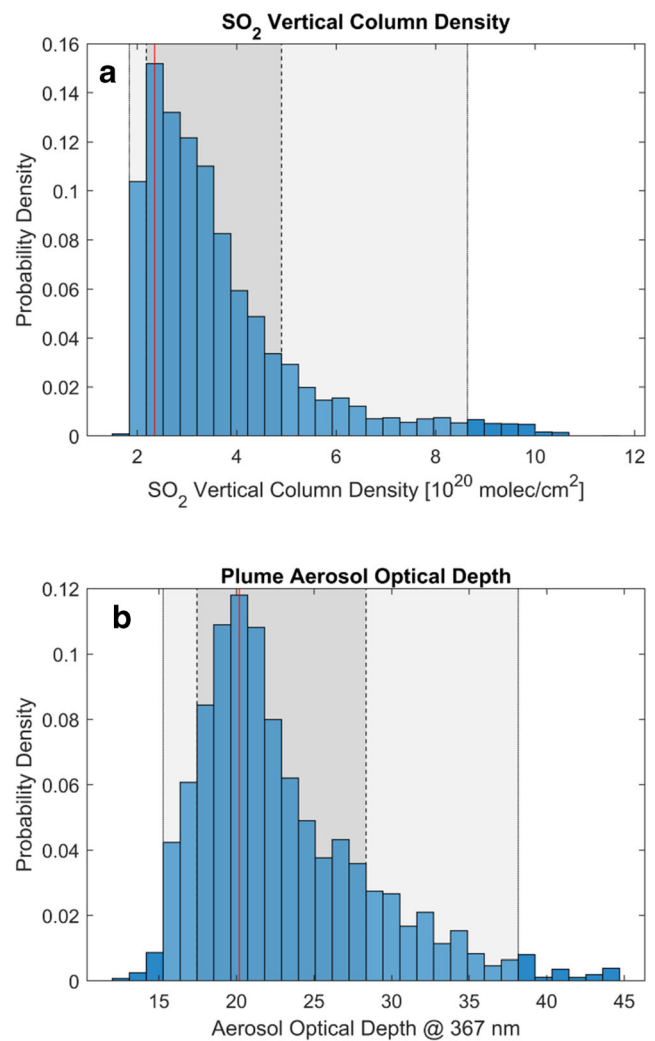

Fig. 8 Example results from the MCMC processing routine applied to the spectrum shown in Fig. 6. The histograms show the probability of various plume conditions being present, given the measured SO_2 SCD and darkening ratio I_p/I_0. The mode of each distribution is given by a red vertical line. The dark gray– and light gray–shaded regions correspond to the 68% and 95% confidence intervals, respectively

obtained while traversing beneath the plume center. However, as the instrument was moved farther towards the plume edges, the distributions became more symmetrical, indicating a higher relative likelihood for light passing straight through the more dilute plume as opposed to around it, but also an increased probability of multiple scattering causing light path extension.

One way to parameterize the distribution is by calculating its confidence intervals. Assuming our retrieved distributions are all unimodal (which they appear to be based on manual spot checks), the 68% and 95% confidence intervals can be calculated for each histogram by integrating the PDF from the mode outward until the respective probability is encompassed in the integration interval. The dark-shaded areas in Fig. 8 show the interval associated with 68% probability, and the light gray areas encompass 95% of the results. These intervals

correspond to the 1σ and 2σ standard deviations of a normal distribution but, in this more general case, can be asymmetrically distributed around the mode.

Figure 8 b shows that the retrieved mode of the AOD PDF was 20 for this measurement spectrum, with values between 18 and 28 lying within the 68% confidence bounds. In general, we found that the width of the AOD distribution was correlated to the assumed uncertainty of the aerosol SSA. Higher assumed values for the plume aerosol SSA required higher AODs in order to explain the dark conditions beneath the plume. An independent measure of SSA would be needed to reduce the uncertainty in our estimates of the plume AOD.

Integrating vertical column densities to obtain emission rates

Once the SO_2 VCD probability distribution was determined for each spectrum, calculating SO_2 emission rates followed the standard mobile DOAS procedures (e.g., Galle et al. 2002; Kantzas and McGonigle 2008; Platt and Stutz 2008). We used a self-developed MATLAB code called "mDOAS" for the spatial analyses. First, the measured VCDs were integrated spatially along the vehicle's track. The wind direction was obtained by fitting a Gaussian curve to the VCDs, then determining the trajectory from its peak to the known vent location. The wind direction error was determined from the 1σ width of the Gaussian. The wind speed at the plume location was taken from the operational output of the Vog Measurement and Prediction (VMAP) project (Businger et al. 2015). For each traverse, the SO_2 emission rate was finally determined by multiplying each VCD segment with the perpendicular component of the wind speed, then spatially integrating all segments along the traverse.

Figure 9 a shows an example traverse acquired on 13 June 2018 (HST). Integration along this track perpendicular to the plume direction yields 8.44×10^{27} SO_2 molecules per lateral meter of plume, which corresponds to 896 kg (SO_2)/m. When multiplied by the VMAP plume speed of 5.5 m/s, we obtain an SO_2 emission rate of 426 kt/day. The same calculation was then performed using the 68% and 95% confidence bounds of the SO_2 VCD distribution at each location along the traverse (shown in gray in Fig. 9b). When combined with the assumed errors of the wind direction and wind speed (standard errors of $\pm 10°$ and ± 1 m/s here), the confidence bounds of each emission rate were determined. In this example, the 68% confidence interval extends from 319 to 528 kt/day, and the 95% confidence interval encompasses the range from 237 to 684 kt/day.

For this traverse, the SCD retrieved in the 345–390-nm-wavelength window (blue line in Fig. 9b) matched the VCD reasonably well indicating that, at these wavelengths, the light path length inside the plume was similar to that of a straight line. Just south of the main plume, the SCD slightly exceeded
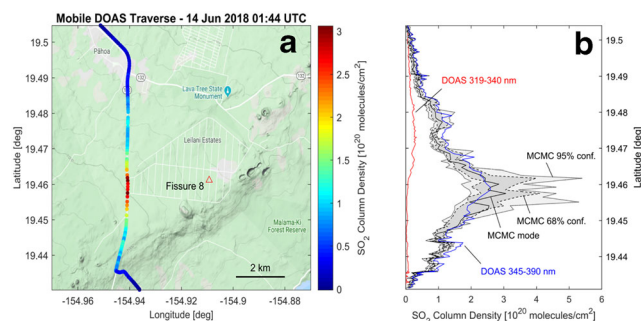

Fig. 9 **a** Example mobile DOAS traverse beneath the fissure 8 plume acquired on 14 June 2018 between 01:39 and 01:49 UTC. The color scale corresponds to the most probable SO_2 VCD above the instrument at each location along the vehicle track, as retrieved using the MCMC method. Map data: Google. **b** Calculated from the histogram of possible VCDs obtained from the MCMC algorithm, the mode, 68% confidence interval, and 95% confidence interval of the output histogram for the VCD are shown in black, dark gray, and light gray, respectively. For comparison, the SCDs obtained by DOAS retrievals performed in the 319–340-nm- and 345–390-nm-wavelength windows are shown in red and blue, respectively

the MCMC confidence intervals, suggesting that multiple scattering within the plume may have increased the light path length here. Note, however, that the SO_2 SCD retrieved in the 319–340-nm interval severely underestimated the VCD for the entire traverse because SO_2 absorption was so strong at these wavelengths that light could not penetrate the plume. Any light reaching the spectrometer had mostly passed around the plume, resulting in shorter in-plume path lengths and lower SCDs. Though these results are specific to the measurement conditions encountered during this traverse, they are consistent with previous recommendations suggesting that the use of the 345–390 nm wavelength range is far preferable when analyzing severe SO_2 column densities (Bobrowski et al. 2010).

Results and discussion

SO_2 emission rates and cumulative emissions

Applying the methodology described above, we retrieved SO_2 emission rates from all mobile DOAS measurements in Kīlauea's LERZ. We find that measured SO_2 emissions were highly variable, even on relatively short timescales (blue circles in Fig. 10). For example, it was not uncommon for emission rates to vary by a factor of 2 or more between individual traverses collected within tens of minutes of one another. This observation is consistent with similar variations in lava effusion rate and infrasound energy occurring on timescales of minutes to hours in June–August (Patrick et al. 2019a).

However, the detected variability is also at least partly due to turbulent atmospheric processes. The dynamics of plume emission, atmospheric dispersion, and downwind transport would at times cause accumulation of gas into dense clouds.
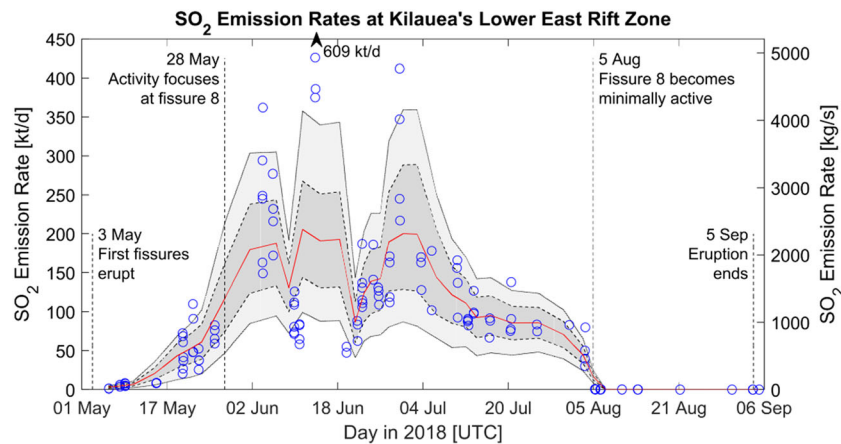
Fig. 10 SO_2 emission rates obtained from mobile DOAS traverses beneath the gas plume emitted at Kīlauea's lower East Rift Zone in May–September 2018. Blue circles depict emission rates obtained from individual traverses (given in Online Resource 2 attached to this article). The red line represents the sustained emission rate, calculated from a running mean of results from three successive days on which measurements were made (given in Online Resource ESM3; see text for details). The shaded areas show the 68% (dark gray) and 95% (light gray) confidence intervals of the sustained emission rates. The black arrow represents a single traverse that yielded 609 kt/day, the highest instantaneous measurement of the entire series. Lava effusion ended on 5 August, although residual degassing continued at low rates for several more weeks

These would then drift downwind in visible puffs. Thus, a traverse transecting beneath one of these puffs would result in an SO_2 emission rate higher than the time-averaged mean whereas a traverse between puffs would underestimate the time-averaged emission rate. Unfortunately, we cannot distinguish between variability in source strength and turbulence-induced variability and therefore cannot easily link short-term variations in our DOAS observations to volcanic processes.

Focusing on longer-term trends, we must consider the relatively long and unequal repeat interval of the traverse measurements. While every effort was made to perform DOAS traverses on as many days as possible, unsuitable weather conditions were frequent such that in the end, the average repeat cycle for the measurements was approximately 3 days. On days when measurements were made, an average of 3.75 successful traverses were obtained in rapid succession, typically within about 90 min. In order to prevent extrapolation of possibly unrepresentative results for periods of several days, we calculated a running mean of most likely SO_2 emission rates (each corresponding to the mode of the respective distribution), with each mean value encompassing all results obtained within three successive days on which measurements were made (red line in Fig. 10). From here on, we will refer to these as *sustained* emission rates to distinguish them from our measurements of the highly variable instantaneous overhead SO_2 burdens and emission rates. We then derived 68% and 95% confidence intervals on the sustained emission rates by calculating the mean confidence intervals from our probability distributions of instantaneous emissions (Fig. 10). Calculated and displayed in this manner, our results characterize the peak, width, and slightly asymmetric shape of the probability distribution of the SO_2 emission rates over time.

SO_2 emissions from the LERZ began concomitantly with the first fissures opening on 3 May and, on 20 May, had reached about 50 kt/day. Note that this already represents an increase by approximately an order of magnitude over the 2014–2017 average emission rate of 5.1 kt/day from Kīlauea's summit and MERZ (Elias et al. 2018) and is more than twice the maximum flux ever measured at the summit during the 2008–2018 activity (Beirle et al. 2014). SO_2 emissions continued to increase further as activity focused at fissure 8 and, by the beginning of June, had reached about 200 kt/day. This extreme level of degassing was sustained for approximately 1 month, with only two brief dips to below 150 kt/day measured on 10 and 20–22 June. SO_2 emissions systematically decreased throughout the month of July, reaching 50 kt/day on 3 August. Lava effusion rapidly decreased the next day (Neal et al. 2019), and on 5 August, SO_2 emission rates had dropped sharply to below 0.5 kt/day. With lava effusion ending, residual SO_2 emissions continued to drop throughout the month of August and reached < 0.01 kt/day in early September.

Integrating the time-averaged SO_2 emissions over the entire period of our measurements (Fig. 11), we derive a most likely cumulative erupted SO_2 mass of 10.2 Mt. Released in only 3 months, this is almost four times greater than the total annual anthropogenic SO_2 emission from the entire USA (USA EPA 2019). The 68% and 95% confidence ranges for the cumulative SO_2 emission estimate are 7.1–13.6 Mt and 4.8–17.0 Mt, respectively. About half of the total SO_2 mass (5.1 Mt) was erupted in the month of June alone, while emissions in May and July amounted to 1.8 Mt and 3.2 Mt, respectively.

Though larger than anthropogenic emissions in the USA, the total SO_2 mass emitted from the LERZ during the 2018

Fig. 11 Cumulative SO₂ emissions from Kīlauea's lower East Rift Zone. The centerline shows the cumulative tonnage assuming the 3-day running mean (red line in Fig. 10) is representative of emissions between measurement days. The shaded areas represent the 95% (light gray) and 68% (dark gray) confidence bounds. Lava effusion largely ended on 5 August, and the last visible lava was observed on 5 September. The most likely cumulative SO₂ tonnage for the entire eruption was 10.2 Mt. See text for details
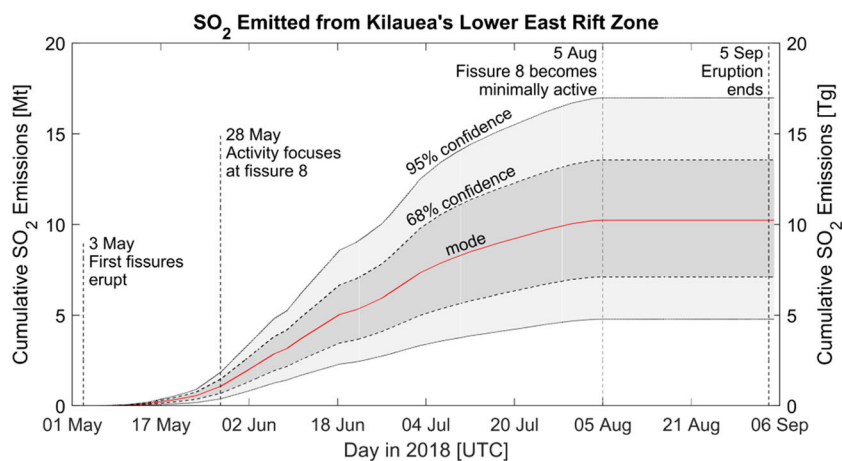
fissure eruption was comparable to the 6.7–14.3 Mt emitted during the 2014–2015 Holuhraun eruption at Bárðarbunga volcano in central Iceland (Pfeffer et al. 2018). The observed maximum sustained LERZ SO₂ emission rate of 200 kt/day was also very similar to that of the Holuhraun eruption (Pfeffer et al. 2018; Carboni et al. 2019), which had widespread impact on the natural environment up to great distances from the eruptive center (Gíslason et al. 2015). However, the total SO₂ mass was emitted from the LERZ eruption in only 3 months rather than the 6 months during which Holuhraun was active (Simmons et al. 2017; Pfeffer et al. 2018).

Viewed in a global volcanic context, the fissure eruptions of Bárðarbunga and Kīlauea volcanoes each added almost 50% to the annual average passive volcanic SO₂ emissions, as observed from satellite instruments (Carn et al. 2017). During their respective eruptions, these two volcanoes each emitted about twice the annual SO₂ mass of the next largest emission source of any kind detected during the 2005–2014 time window (Ambrym volcano emitted ~ 4.6 Mt in 2010; Fioletov et al. 2016). In fact, each of these two eruptions emitted about half the SO₂ mass of the largest volcanic eruption of the past century: the 1991 explosive VEI-6 eruption of Mount Pinatubo, which released ~ 20 Mt of SO₂ (Guo et al. 2004). However, the Pinatubo eruption explosively injected most of its SO₂ into the stratosphere where it formed sulfate aerosols that remained there for years and had significant global climate impact (McCormick et al. 1995; Soden et al. 2002).

Emitting SO₂ into the low-level troposphere, Bárðarbunga and Kīlauea are therefore perhaps better compared to the 2000–2002 caldera-forming eruption of Miyakejima volcano in Japan. During the 2-year eruption, Miyakejima emitted about 18 Mt of SO₂ into the troposphere, leading to sustained hazardous gas concentrations in residential areas along the coast (Shinohara et al. 2003; Kazahaya et al. 2004; Matsushima 2005). Although larger than Kīlauea's 2018 eruption in cumulative SO₂ output, Kīlauea's sustained SO₂ emission rate of ~ 200 kt/day was four times larger than the 40–50

kt/day emitted during Miyakejima's most active period (Kazahaya et al. 2004). Even when emitted into the troposphere where sulfate aerosols are removed much more quickly than in the stratosphere, SO₂ emissions of this magnitude can have regional effects on climate and meteorology (Eguchi et al. 2011; Uno et al. 2014).

Emission of other gases

The SO₂ emissions associated with the 2018 fissure eruption at Kīlauea were among the largest observed anywhere in the world for the past many years. Combined with measurements of relative plume composition, we can extrapolate cumulative emissions of other gases as well.

Water vapor is the most abundant magmatic volatile species and, in Hawaiian basalts, usually contributes about 75% of all emitted gas (Gerlach 2004). Water vapor measurements were performed with MultiGAS mounted on unoccupied aircraft systems (UAS) which were flown into the gas plumes directly above the active fissures in the LERZ (Clor et al. 2018; Kelly et al. this issue). The resulting H₂O/SO₂ molar ratios typically ranged between about 4 and 6 with an average of 5.4. Assuming this ratio as approximately representative for the entire eruptive episode, we obtain a sustained volcanic H₂O flux of about 300 kt/day in June and July, and a total cumulative water vapor emission of between 11 and 21 Mt at the 68% confidence interval. Emitted from a point source, this represents a significant injection of water vapor and especially latent heat into the troposphere, which, on many days, resulted in formation of pyrocumulus clouds directly over the active fissure(s) in the LERZ. However, viewed in the context of the regional hydrological cycle, the H₂O flux is relatively minor. Evaporation rates from the equatorial Pacific Ocean average about 5.5 mm/day (Babkin 2009). Therefore, the sustained volcanic H₂O flux into the atmosphere in June and July was approximately equivalent to the coincident evaporation from a nearby 54-km² parcel of ocean.

Also measured by MultiGAS, the CO_2/SO_2 molar ratio in the LERZ gas remained remarkably constant at ~ 0.30 throughout the eruption (Clor et al. 2018; Kelly et al. this issue). This composition is consistent with that of a Kīlauea "type II" volcanic gas as described by Gerlach (1986), indicating that the majority of CO_2 was likely degassed prior to eruption of the lava. Historically, CO_2-rich "type I" gases have been emitted at Kīlauea's summit which is spatially aligned with the volcano's deep plumbing system where CO_2 exsolves (Gerlach 1986). Typical deep magma supply has been associated with summit CO_2 emission rates in the range of 5–25 kt/day since 1995 (Gerlach et al. 2002; Sutton and Elias 2014). By scaling our SO_2 emissions with the CO_2/SO_2 ratio, we can only calculate the CO_2 mass emitted from the LERZ during the eruption. Acknowledging that this approach misses previous CO_2 degassing and degassing that may be occurring elsewhere on the volcano, we estimate LERZ CO_2 emissions were between 1.5 and 2.8 Mt at the 68% confidence interval, with a time-averaged CO_2 emission rate of about 40 kt/day sustained during the maximum degassing activity in June and July. Note that this is lower than the 3.6–7.6 Mt emitted during the Holuhraun eruption (Pfeffer et al. 2018), which may again be attributable to the partially degassed nature of the LERZ magma. The State of Hawai'i's annual anthropogenic CO_2 emissions are about 20 Mt (DOH 2019), so despite the extreme degassing associated with the LERZ eruption, the event only added about 10% to this total in 2018. Viewed in a global context, Kīlauea's LERZ CO_2 emissions corresponded to about 1% of the estimated 140–300 Mt CO_2 emitted by global subaerial volcanism in an average year (Fischer et al. 2019; Werner et al. 2019) and were dwarfed by the > 40,000 Mt CO_2 released by anthropogenic activities each year (IPCC 2014).

Throughout the eruption, sulfur was almost exclusively emitted from the active fissures in the LERZ in the oxidized form of SO_2. Based on the detection limit of our UAS-mounted MultiGAS instrument, the H_2S/SO_2 molar ratio remained below about 0.06. Besides SO_2 and H_2S, we also checked for the presence of carbon disulfide (CS_2) in the gases emitted from the LERZ using our DOAS data. Passive DOAS has a limited sensitivity to the differential absorption of CS_2 in the 300–350-nm-wavelength region. However, we were not able to detect light absorption by CS_2 in any of our measurements despite the very large SO_2 abundances. Again, considering the detection limit of our instrument, we find that the CS_2/SO_2 ratio in the gas plume remained below 0.01, at least during the period of greatest SO_2 emissions in June and early July, which is consistent with measurements at other volcanoes yielding only very minor CS_2 emissions (Textor et al. 2004). Note that small amounts of hydrothermal gases including H_2O, CO_2, SO_2, and H_2S were emitted in less active areas on the periphery of the eruptive fissures (Clor et al. 2018). However, emission rates from these sources were negligible compared to the active fissures themselves and below the detection limits of the DOAS instrumentation.

Finally, we attempted to retrieve column densities of the halogen oxides bromine monoxide (BrO) and chlorine dioxide (OClO) in the DOAS spectra. These gases are secondary products that form when the halogen halides HCl and HBr in volcanic gases are oxidized in heterogeneous chemical reactions occurring on aerosol particle surfaces (e.g., Bobrowski et al. 2003, 2007; Oppenheimer et al. 2006; Gutmann et al. 2018). The extreme overhead gas burdens resulted in a highly sensitive measurement of the X/SO_2 ratios and, for the first time, allowed us to detect BrO in gas emitted from Kīlauea Volcano. During the period of highest emissions in June, the BrO/SO_2 ratio was approximately 3.5×10^{-6} when measured 3 km downwind of the active vent at a plume age of about 9 min. This ratio is approximately an order of magnitude lower than values typical for arc volcanoes (Gutmann et al. 2018), but comparable to ratios previously measured at the Nyiragongo and Nyamuragira volcanoes in the East African Rift System (Bobrowski et al. 2017a, 2017b). The low BrO/SO_2 ratio is also consistent with Kīlauea's relatively low bromine emission budget (Mather et al. 2012) and only minor levels of ozone depletion measured in downwind areas (Roberts 2018). OClO column densities were below our detection limit throughout the eruption. Based on the noise level of our measurements, the $OClO/SO_2$ ratio remained below 3×10^{-6} molecules/cm^2. Details of our BrO and OClO analysis methods are given in Online Resource 6 attached to this article.

SO_2 emissions from Kīlauea's summit and East Rift Zone during the LERZ eruption

During the 2018 fissure eruption, SO_2 emissions from Kīlauea's LERZ by far exceeded those from other source areas on the volcano. This represents a significant change in the distribution of emissions at Kīlauea, as the volcano's summit had been the most prodigious gas source for a decade since the opening of the Halema'uma'u Summit Overlook Vent in 2008. Initially reaching as high as ~ 20 kt/day in 2008 (Beirle et al. 2014), SO_2 emissions from the summit had averaged 4.8 kt/day in the 2014–2017 period (Elias et al. 2018). Summit emissions continued at this rate during the onset of the 2018 LERZ eruption (Fig. 12a). Then, several minor explosions occurred at the summit from 16 to 26 May, with the largest event on 17 May sending gas and ash up to 8 km above ground level (Neal et al. 2019). Fortuitous measurement timing allowed us to capture a spike in SO_2 emission rate associated with explosions on 23 May. As the Halema'uma'u Crater had become too hazardous to approach by this time, DOAS traverses were made by hiking on the Mauni Iki Trail, approximately 7 km downwind of the summit vent. Two traverses made during visually observed explosive activity on that day yielded emission rates of 10 kt/day and 13

Fig. 12 Daily average SO$_2$ emission rates measured at Kīlauea's summit vent (**a**) and MERZ (**b**) during the 2018 LERZ eruptive episode. The high emission rates measured on 23 May downwind of the volcano's summit were associated with explosive activity.
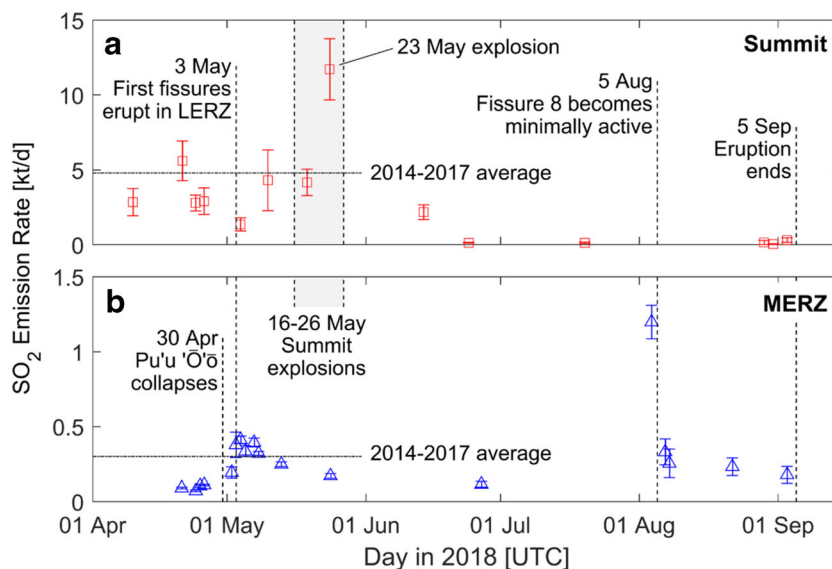
kt/day, respectively. Though our dataset is admittedly sparse, these measurements appear to indicate that SO$_2$ emissions from the summit increased by a factor of 2–3 above background values during summit explosions.

As previously noted by Neal et al. (2019), this finding is not consistent with a suggested model developed by Stearns (1925) during Kīlauea's last summit explosive activity in 1924 in which the infiltration of groundwater into the hot conduit of the collapsing summit vent caused explosions (also see Hsieh and Ingebritsen 2019). Such phreatic blasts would not generally be associated with increased SO$_2$ emissions. Rather, interaction of gases with water could cause scrubbing of SO$_2$ and/or conversion of SO$_2$ to H$_2$S and might decrease SO$_2$ emissions (Symonds et al. 2001). Our measurements of elevated SO$_2$ emissions during explosive events suggest that the explosions may instead have been caused by debris falling into the crater. Gas accumulating beneath and then surging through a layer of debris could cause lithic-rich explosions similar to those described by Houghton et al. (2011). Decompression of the magma remaining in the shallow summit reservoir as it was tapped from below by the effusive eruption in the LERZ may also have allowed sulfur to partition into the gas phase more efficiently and at greater depth below the surface than was previously the case. Some combination of these processes likely caused the May explosions at the summit.

Although our dataset is sparse, our measurements indicate that SO$_2$ emissions likely averaged 1–4 kt/day from the summit during the period of steady caldera collapse. During this time, the Halema'uma'u vent became progressively choked with collapse debris, presumably re-pressurizing the shallow magma storage area and inhibiting SO$_2$ exsolution. At the time of writing (June 2020), summit SO$_2$ emissions have dropped to < 50 t/day and a small crater lake has formed within the collapsed crater.

In addition to the summit emissions, an average of ~ 300 t/day of SO$_2$ were being emitted from the Pu'u 'Ō'ō cone and surrounding area in Kīlauea's MERZ during the 2014–2017 period (Elias et al. 2018). Interestingly, emissions from this source dropped to only about 100 t/day in late April 2018 (Fig. 12b), coincident with inflationary ground deformation at Pu'u 'Ō'ō (Neal et al. 2019; Patrick et al. 2020), suggesting pressurization of the system. A constriction in the shallow plumbing system of the ERZ may have been impeding normal magma migration/convection patterns (Orr et al. 2015; Patrick et al. 2019b, 2020). Or perhaps, a relatively degassed viscous layer of shallow magma established itself at the top of the plumbing system, hindering efficient magma turnover and surface degassing. Pu'u 'Ō'ō began collapsing on 30 April 2018, and measurements made shortly thereafter on 4 May showed that SO$_2$ emissions from the ERZ initially rebounded to the 300–400 t/day range. However, subsequent measurements show that, with the exception of a brief spike measured in early August, the emission rate has dropped slowly over months to below the detection limit of our instruments (< 20 t/day). All SO$_2$ emission rates measured at Kīlauea's summit and MERZ during the April–September 2018 timeframe are given in Online Resources 4 and 5 attached to this article.

Implications for air quality on Hawai'i Island

The 2018 LERZ eruption had serious and detrimental impacts on air quality for much of the state of Hawai'i. SO$_2$ emissions were so great that they briefly impacted air quality as far away as Guam, some 6000 km away (GHS/OCD 2018). Air quality forecasts played an important role in alerting emergency managers and the public to episodes of poor air quality. Since 2011, the VMAP project has been producing real-time forecasts of SO$_2$ and volcanogenic sulfate aerosol (SO$_4$) through use of the Hybrid Single Particle Lagrangian Integrated Trajectory (HYSPLIT) model (Businger et al. 2015). In January 2017, the VMAP implementation of HYSPLIT began

using a custom WRF-ARW (Weather and Research Forecast model – Advanced Research WRF core) numerical weather forecast with a domain that covers the state of Hawai'i at 900 m horizontal resolution. As a transport and dispersion model, HYSPLIT uses these high-resolution WRF-ARW meteorological forecasts to forecast hourly averages of SO_2 and SO_4 concentrations for 60 h into the future twice per day (00:00 and 12:00 UTC initialization times) based on a 27-member ensemble. The average of the ensemble (ensemble mean) produces a more skillful forecast than a single forecast based on the same underlying model can produce (for details, see Holland et al. 2020).

HVO provides up to date SO_2 emission rates for use in the VMAP forecast. The SO_2 emission rate is among the most important inputs to the VMAP forecasts and has direct implications for overall forecast quality (Holland et al. 2020). Unsurprisingly, the drastic increase in SO_2 emission rate along with the shift in primary source location from Kīlauea's summit to the LERZ associated with the 2018 rift eruption significantly affected air quality. To illustrate the impact of the LERZ eruption in more detail, we first initialized the forecast model beginning at 00:00 UTC on 6 June 2018 assuming 4800 t/day SO_2 emitting from the volcano's summit and 300 t/day being released from the Pu'u 'Ō'ō vent. These values correspond to the mean emissions during the 2014–2017 time period (Elias et al. 2018). The results of this hypothetical scenario are shown in Fig. 13 a.

This forecast is then compared to a simulation initialized on the same day with the most likely SO_2 emission rates at that time according to our measurements. Using our best estimate of sustained SO_2 emissions on 6 June 2018, this VMAP forecast was initialized with 188,000 t/day SO_2 emitted from fissure 8 in the LERZ, 2200 t/day SO_2 emitted from the summit, and 100 t/day emitted from Pu'u 'Ō'ō. Figure 13 b shows the near-surface SO_2 concentrations forecast for this scenario.

The eruption's impact on air quality in Hawai'i becomes clear when comparing the two VMAP forecasts. The area in which near-surface SO_2 concentrations are expected to exceed the OSHA exposure limit of 5 ppmv was significantly larger during the LERZ eruption than was previously the case. In our example, the area in which mixing ratios exceeded 1 ppmv, a value classified as "unhealthy" by the Hawai'i Department of Health (HDOH 2011), encompassed a significant portion of Hawai'i Island's Ka'ū District and extended all the way to the island's southern tip. Also modeled by VMAP, the conversion of SO_2 to sulfate aerosols led to increased aerosol concentrations throughout all downwind regions. Unhealthy levels of particulate matter from sulfate aerosols forming in the downwind plume were common throughout southern Hawai'i Island and on the Kona Coast, the island's most popular tourist region, throughout May, June, and July 2018 (Whitty et al. 2020).

Exposure to a combination of SO_2 and sulfate aerosols (vog) has been linked to a variety of respiratory symptoms,

depending on concentration and exposure duration (Tam et al. 2016 and references therein). During the eruption, information on historical and real-time air quality from a variety of sources was available to the public through the International Volcanic Health Hazard Network's Hawai'i Interagency Vog Information Dashboard (vog.ivhhn.org). A more detailed analysis of the 2018 eruption's environmental impact is the topic of ongoing research.

Estimating lava effusion volume from SO_2 emissions

SO_2 emission rates have been used to determine lava effusion rates at Kīlauea for decades, particularly during the 1983–2008 Pu'u 'Ō'ō eruption period when all erupted lava and most SO_2 gas were emitted at the Pu'u 'Ō'ō vent. This circumstance allowed a direct comparison of SO_2 emission rates and lava effusion and showed that SO_2 emission rates could be used to estimate erupted lava volume for Kīlauea (Sutton et al. 2003). The 2018 LERZ eruption represents a similar situation of co-located gas and lava effusion. Based on petrologic degassing models for Kīlauea (Gerlach 1986; Moussallam et al. 2016; Lerner et al. this issue; Kelly et al. this issue), sulfur does not significantly exsolve from Kīlauea magma until it has ascended to very shallow depths (< 100-200 m) where pressures are < 2-5 MPa. The high sulfur solubility in Kīlauea's magmas stems from these melts being high-temperature, iron-rich, and relatively water-poor, the latter of which prevents high degrees of mixed volatile (C-H-S) degassing from greater depths (Gerlach 1986; Dixon et al. 1995; Fortin et al. 2015).

These sulfur-degassing calculations are consistent with the low SO_2 emission rates (< 200 t/day) observed at Kīlauea's summit during times of eruptive quiescence there, such as prior to 2008 (Elias and Sutton 2002, 2007). Efficient degassing of unerupted magma could only occur if this magma were brought to depths of less than ~ 200 m below the surface to degas before then being stored underground. Such shallow magma convection is unlikely in an open system in which lava is vigorously being erupted from active fissures, as was the case for the 2018 LERZ eruption. Storage of a significant magma volume at relatively shallow depth would also cause local surface deformation. Geophysical measurements reported by Neal et al. (2019) did capture the intrusion of magma into a dike beneath the LERZ, but the emplaced volume was estimated to 0.08 km^3 which, as we will show, is less than 5% of our estimated lava effusion volume. The contribution of SO_2 degassing from unerupted LERZ magma is therefore considered negligible compared to the large SO_2 emissions associated with the very high lava effusion rates, and for the following calculations, we assume that all degassed magma was erupted.

Making a further simplifying assumption that the main fissure 8 stage of the LERZ eruption was fed by primary Kīlauea
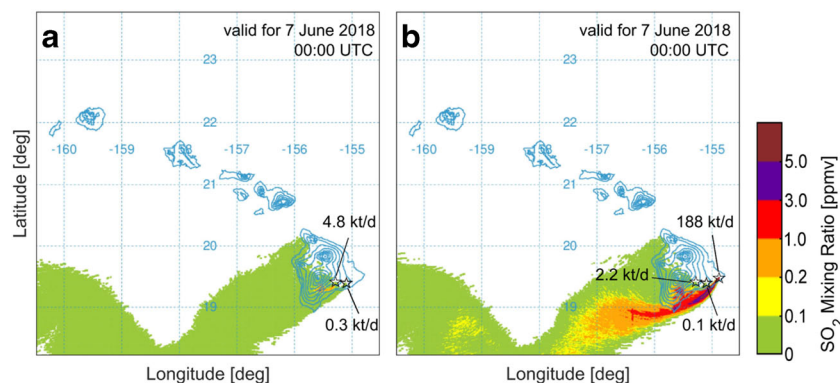
Fig. 13 Comparison of two VMAP ensemble mean forecasts of near-surface SO_2 concentrations illustrating the impact of the 2018 LERZ eruption on air quality. Both images show the conditions forecast for 00:00 UTC on 7 June 2018 based on model initialization at 00:00 UTC on 6 June 2018. The forecast shown in **a** was calculated using a hypothetical scenario in which SO_2 emissions correspond to the mean values from the 2014–2017 period: 4.8 kt/day SO_2 from the summit and 0.3 kt/day from Pu'u 'Ō'ō (Elias et al. 2018). The forecast shown in **b** was calculated using the actual sustained SO_2 emissions from 6 June 2018 according to our measurements: 2.2 kt/day from the summit, 0.1 kt/day from Pu'u 'Ō'ō, and 188 kt/day from fissure 8 in the LERZ. Stars indicate the locations of the individual emission sources

magma that did not lose significant amounts of sulfur on its way to the surface, the erupted lava likely contained between 1200 and 1500 ppm sulfur (Rowe et al. 2015; Thornber et al. 2015). Wieser et al. (2020) estimate the sulfur content at sulfide saturation (SCSS) limit of Kīlauea lavas to be around 1250 ppm. This value also agrees well with SCSS calculations based on the model of Fortin et al. (2015) for fissure 8 melt conditions (temperature, iron content, oxygen fugacity) and is also consistent with the upper range of sulfur concentrations measured in LERZ melt inclusions (Lerner et al. 2019, this issue), so we adopt this value in our estimates below.

Assuming a bubble-free lava density (ρ) of 2.7 t/m^3 calculated from fissure 8 melt compositions (Lerner et al. this issue) and that sulfur completely degasses from the melt, the dense-rock equivalent volume of extruded lava can be estimated from the total emitted SO_2 mass (M_{SO_2})

$$V = \frac{M_{SO_2}}{2c_s\rho} \cdot (1 - f_{xtl})^{-1} \tag{5}$$

where c_s is the melt's sulfur concentration, the factor of 2 accounts for the fact that only half the mass of emitted SO_2 corresponds to that of sulfur, and f_{xtl} is the sulfur-free crystal fraction of the erupting magma. For these calculations, we assume $f_{xtl} \approx 0.1$ in the bubble-free magma, consistent with analyzed samples of fissure 8 lavas (Gansecki et al. 2019; T. Shea, personal communication). Finally, inserting our estimated 10.2 Mt of SO_2 emitted during the 2018 eruption, Eq. (5) yields an erupted dense-rock equivalent volume of 1.7 km^3. Assuming our petrologic degassing model is correct and our initial sulfur concentration of the LERZ melts is accurate to within 15%, the 68% and 95% confidence intervals for the erupted lava volume are 1.1–2.3 km^3 and 0.8–2.8 km^3, respectively.

Despite the uncertainty, our calculations yield a > 95% likelihood for the erupted magma volume having been larger than the summit caldera collapse volume estimate of 0.8 km^3 determined using geophysical methods (Anderson et al. 2019; Neal et al. 2019). This suggests that the shallow summit reservoir was not the sole source of magma feeding the eruption. Instead, magma previously stored in the ERZ and south caldera reservoir likely contributed a significant portion of the erupted volume. This is consistent with geodetic measurements of syn-eruptive deflation in these locations (Anderson et al. 2019; Denlinger 2019; Neal et al. 2019; Patrick et al. 2020) and the petrologically estimated depths of magma storage (Lerner et al. this issue). Our best estimate of 1.7 km^3 is also consistent with estimates of lava effusion based on the geometries and velocities of subaerial lava flows during the months-long period of lava ocean entry (Dietterich et al. 2019, this issue).

Future work

The developed MCMC inversion of volcanic plume conditions and SO_2 emission rates is applicable to other DOAS measurements of opaque plumes. However, it will not be possible to use the same measured data products (SO_2 SCD at 345–390 nm and I_p/I_0 at 367 nm) in situations with less severe gas emissions. One area of future study will therefore be to test this approach in more common measurement conditions with weaker plumes.

In general, the uncertainty of the retrieved SO_2 emission rates and plume AODs could also be improved by providing the MCMC algorithm with additional information on the physical state of the plume and atmosphere. This includes information on the exact location and extent of the plume, as well as information on conditions inside the plume. In this context, two parameters would be particularly useful. First, better constraints on the aerosol SSA in the volcanic plume

would immediately focus the algorithm on a more realistic set of possible plume conditions. Second, obtaining independent information on the Ångström exponent would be of great value. The Ångström exponent describes the wavelength dependency of aerosol scattering processes and primarily depends on the effective radii of the aerosol particles (Ångström 1929). Knowledge of this parameter would allow the development of a unified retrieval that takes information from a wider spectral range into account, e.g., utilizing the SO_2 SCDs measured at 319–340 nm along with those measured at 345–390 nm.

The information content provided by oxygen dimer (O_4) absorption also deserves further consideration, as this parameter can be measured by the DOAS systems directly. In atmospheric DOAS applications, O_4 SCDs are often used as a measure of light path length (Wagner et al. 2004; Frieß et al. 2006). However, contrary to the anticipated behavior, we found our measured O_4 SCDs to be anti-correlated with retrieved light path length in the plume (AMF). Initial model results seem to indicate that, for the extremely dense plumes encountered here, a significant contribution of the measured signal comes from light entering the spectrometer's field of view at low elevation angles. This radiation is scattered in the lower regions of the plume and therefore does not have to pass through its center to reach the spectrometer. However, because this light passes through the lower atmosphere at an oblique angle, it carries a much higher O_4 absorption signal than light passing through the plume from above. This atmospheric effect appears to dominate the O_4 absorption signal over any pathlength-extension effects occurring inside the plume.

The increased use of UAS for volcanic gas measurements is of great promise, both for improving upon our methodology and for performing validation experiments (James et al. 2020). Equipped with simple cameras, UAS flying around a volcanic plume can precisely constrain its location and extent (Wood et al. 2019). If flown within the plume, measurements of the particle size distribution, aerosol composition, and scattering and absorption properties could inform our assumed aerosol SSA and Ångström exponents (Mori et al. 2016; Rüdiger et al. 2018; Stix et al. 2018). Results of our integrated column SO_2 measurements could also be compared with in situ measurements, for example if UAS carrying an SO_2 sensor were flown vertically through a dense gas cloud coincident with upward-looking DOAS observations along the approximate flight path. Unfortunately, though near-field UAS measurements were made (Whitty et al. 2019; Ilyinskaya et al. 2020; Mason et al. 2020; Kelly et al. this issue), we could not obtain the necessary permissions to fly a UAS vertically through the LERZ plumes at the DOAS traverse location in 2018 due to concerns of losing sight of the aircraft, possible disruption of the telemetry link between the UAS and the ground crew

caused by the high aerosol load, and the aircraft leaving the designated low-level airspace in which a temporary flight restriction for drone operations was in place.

Finally, satellite observations may provide another useful means for validating our results. As satellite measurements are also remote sensing observations, they are subject to some of the same limitations as our own measurements. In particular, UV satellite sensors like OMI, OMPS, and TROPOMI are susceptible to underestimating the SO_2 load if the radiative transfer in and around dense, low-altitude volcanic plumes is not properly accounted for, so it is perhaps not surprising that operational SO_2 products tend to yield values lower than ours (see Vernier et al. 2020, Tang et al. 2020 for some examples). However, while we were restricted to making measurements on existing roads, satellites can track the gas plume for hundreds of kilometers downwind. Moving farther downwind allows for measurements of optically thinner plumes which simplifies the spectroscopy. Though the issue of SO_2 conversion to sulfate in the downwind plume must be taken into account, examination of the SO_2 burden as a function of distance could provide the required information on SO_2 removal (Beirle et al. 2014). Independent information could also be obtained by examining satellite products in both the UV and IR spectral bands, as each has their own limitations and advantages (Carn et al. 2016). In particular, the unprecedented spatial resolution of the new TROPOMI UV satellite instrument could provide a means of validation and comparison (Theys et al. 2019). Similarly, new techniques for retrieving SO_2 column densities from ASTER, VIIRS, and MODIS infrared imagery could provide complementary information (Realmuto et al. 2018). It is our hope that by pursuing these and other similar research avenues, we may be able to further reduce the uncertainty of our measurements in the future.

Conclusions

In May–August 2018, the fissure eruption of Kīlauea Volcano emitted prodigious amounts of volcanic gas and aerosols into the lower troposphere. Visual observations of the gas plumes emitted from active fissures in the LERZ showed that sulfate aerosols were present directly above the active vents, as sunlight scattering on these particles commonly lent a blue or orange tinge to the plume edges. Conditions beneath the plume were often dark, with downwelling radiance decreasing to only a few percent of the values observed away from the plume. This opacity made interpretation of our DOAS measurements challenging and necessitated the development of a statistical inversion procedure.

Applying our novel method, which combines mobile DOAS traverses beneath the gas plumes with radiative transfer modeling, we estimate that between 7.1 and 13.6 Mt of SO_2 were emitted during the course of the eruption.

Instantaneous SO_2 emission rates as high as 609 kt/day were measured in June, and an average emission rate of about 200 kt/day was sustained for more than a month during the period of greatest activity. This makes the 2018 LERZ eruption of Kīlauea Volcano one of the largest in the past two decades in terms of SO_2 output, comparable only to the 2014–2015 Holuhraun and the 2000–2002 Miyakejima eruptions (Pfeffer et al. 2018; Kazahaya et al. 2004). Scaling SO_2 emissions to measured gas ratios, we estimate that 11–21 Mt H_2O and 1.5–2.8 Mt CO_2 were also emitted from the LERZ.

The appearance of intensely degassing volcanic fissures in close proximity to the population and infrastructure of the Puna District led to conditions that at times posed an immediate threat to the life and safety of residents and emergency responders. Variable meteorological conditions changed the conditions in the affected areas with little warning. Further downwind, the LERZ SO_2 emissions also greatly affected air quality throughout southern Hawai'i Island and on the Kona Coast. Using HVO's near-real-time estimates of SO_2 emission rates as input, the VMAP project provided useful air quality forecasts for Hawai'i's residents and visitors.

Our observations also yielded insights into geophysical processes occurring during the eruption. Explosions at Kīlauea's summit appear to have been associated with pulses of SO_2 degassing, indicating that the source mechanism for these events was probably not of phreatic nature but rather a choking of the volatile flux by debris collapsing into the crater and leading to pressurization (Houghton et al. 2011). Based on SO_2 emissions and primary sulfur contents of the magma, estimates of the lava volume erupted in the LERZ (1.1-2.3 km^3) are significantly larger than the summit caldera collapse volume (0.8 km^3). This indicates that significant amounts of erupted lava came from a deeper summit reservoir or from along the ERZ, consistent with models proposed by others (Anderson et al. 2019; Denlinger 2019; Lerner et al. this issue).

References

Allen AG, Oppenheimer C, Ferm M, Baxter PJ, Horrocks LA, Galle B, McGonigle AJS, Duffell HJ (2002) Primary sulfate aerosol and associated emissions from Masaya Volcano, Nicaragua. J Geophys Res Atmos 107. https://doi.org/10.1029/2002JD002120

Ammann M, Burtscher H (1993) Aerosol dynamics and light-scattering properties of a volcanic plume. J Geophys Res 98:19705–19711. https://doi.org/10.1029/93JB02003

Anderson KR, Johanson IA, Patrick MR, Gu M, Segall P, Poland MP, Montgomery-brown EK, Miklius A (2019) Magma reservoir failure and the onset of caldera collapse at Kīlauea Volcano in 2018. Science (80):366, 1–310. https://doi.org/10.1126/science.aaz1822

Ångström A (1929) On the atmospheric transmission of Sun radiation and on dust in the air. Geogr Ann 11:156–166. https://doi.org/10.1080/20014422.1929.11880498

Babkin VI (2009) Evaporation from the surface of the globe. In: Shiklomanov IA (ed) The hydrological cycle - UNESCO encyclopedia of life support systems. 364p.

Barahona D, Breen K, Yuan T, Huisheng B (2019) Effect of volcanic emissions on clouds during the 2008 and 2018 Kilauea degassing events. AGU Fall Meeting Abstracts. https://agu.confex.com/agu/fm19/meetingapp.cgi/Paper/591870. Accessed 9 Jun 2020

Beirle S, Hörmann C, Penning de Vries M, Dörner S, Kern C, Wagner T (2014) Estimating the volcanic emission rate and atmospheric lifetime of SO_2 from space: a case study for Kīlauea Volcano, Hawai'i. Atmos Chem Phys 14:8309–8322. https://doi.org/10.5194/acp-14-8309-2014

Bobrowski N, Hönninger G, Galle B, Platt U (2003) Detection of bromine monoxide in a volcanic plume. Nature 423:273–276. https://doi.org/10.1038/nature01625

Bobrowski N, von Glasow R, Aiuppa A, Inguaggiato S, Louban I, Ibrahim OW, Platt U (2007) Reactive halogen chemistry in volcanic plumes. J Geophys Res 112:D06311. https://doi.org/10.1029/2006JD007206

Bobrowski N, Kern C, Platt U, Hörmann C, Wagner T (2010) Novel SO_2 spectral evaluation scheme using the 360-390 nm wavelength range. Atmos Meas Tech 3:879–891. https://doi.org/10.5194/amt-3-879-2010

Bobrowski N, Giuffrida GB, Arellano S, Yalire M, Liotta M, Brusca L, Calabrese S, Scaglione S, Rüdiger J, Castro JM, Galle B, Tedesco D (2017a) Plume composition and volatile flux of Nyamulagira volcano, Democratic Republic of Congo, during birth and evolution of the lava lake, 2014–2015. Bull Volcanol 79:90. https://doi.org/10.1007/s00445-017-1174-0

Bobrowski N, Giuffrida GB, Yalire M, Lübcke P, Arellano S, Balagizi C, Calabrese S, Galle B, Tedesco D (2017b) Multi-component gas emission measurements of the active lava lake of Nyiragongo, DR Congo. J Afr Earth Sci 134:856–865. https://doi.org/10.1016/j.jafrearsci.2016.07.010

Bogumil K, Orphal J, Homann T, Voigt S, Spietz P, Fleischmann OC, Vogel A, Hartmann M, Kromminga H, Bovensmann H, Frerick J, Burrows JP (2003) Measurements of molecular absorption spectra with the SCIAMACHY pre-flight model: instrument characterization and reference data for atmospheric remote-sensing in the 230–2380 nm region. J Photochem Photobiol A Chem 157:167–184. https://doi.org/10.1016/S1010-6030(03)00062-5

Bouguer P (1729) Essai d'optique sur la gradation de la lumiere. Claude Jombert, Paris

Businger S, Huff R, Pattantyus A, Horton KA, Sutton AJ, Elias T, Cherubini T (2015) Observing and forecasting vog dispersion from Kīlauea Volcano, Hawai'i. Bull Amer Meteor Soc 96:1667–1686. https://doi.org/10.1175/BAMS-D-14-00150.1

Campion R, Delgado-Granados H, Mori T (2014) Image-based correction of the light dilution effect for SO_2 camera measurements. J

Volcanol Geotherm Res 300:48–57. https://doi.org/10.1016/j.jvolgeores.2015.01.004

Carboni E, Mather TA, Schmidt A, Grainger RG, Pfeffer MA, Ialongo I, Theys N (2019) Satellite-derived sulfur dioxide (SO_2) emissions from the 2014-2015 Holuhraun eruption (Iceland). Atmos Chem Phys 19:4851–4862. https://doi.org/10.5194/acp-19-4851-2019

Carn SA, Clarisse L, Prata AJ (2016) Multi-decadal satellite measurements of global volcanic degassing. J Volcanol Geotherm Res 311:99–134. https://doi.org/10.1016/j.jvolgeores.2016.01.002

Carn SA, Fioletov VE, McLinden CA, Li C, Krotkov NA (2017) A decade of global volcanic SO_2 emissions measured from space. Sci Rep 7:44095. https://doi.org/10.1038/srep44095

Clor L, Kelly P, Nadeau P, Lerner A, Elias T, Kern C, Werner C, Diefenbach A, Cappos M (2018) Gas composition monitoring with Multi-GAS during the 2018 eruption of Kīlauea, Hawai'i. AGU Fall Meeting Abstracts. https://agu.confex.com/agu/fm18/meetingapp.cgi/Paper/395417. Accessed 9 Jun 2020

de Moor JM, Aiuppa A, Pacheco J, Avard G, Kern C, Liuzzo M, Martínez M, Giudice G, Fischer TP (2016) Short-period volcanic gas precursors to phreatic eruptions: insights from Poás Volcano, Costa Rica. Earth Planet Sci Lett 1:218–227. https://doi.org/10.1016/j.epsl.2016.02.056

Denlinger R (2019) Anatomy of Kīlauea Volcano. AGU Fall Meeting Abstracts, https://agu.confex.com/agu/fm19/meetingapp.cgi/Paper/487143. Accessed 9 Jun 2020

Deutschmann T, Beirle S, Frieß U, Grzegorski M, Kern C, Kritten L, Platt U, Prados-Román C, Puķite J, Wagner T, Werner B, Pfeilsticker K (2011) The Monte Carlo atmospheric radiative transfer model McArtim: introduction and validation of Jacobians and 3D features. J Quant Spectrosc Radiat Transf 112:1119–1137. https://doi.org/10.1016/j.jqsrt.2010.12.009

Dietterich HR, Patrick M, Diefenbach A, Lundgren P, Cashman K, Grant GE (2019) Lava effusion rates and channel dynamics during the 2018 Kīlauea lower East Rift Zone eruption. AGU Fall Meeting Abstracts. https://agu.confex.com/agu/fm19/meetingapp.cgi/Paper/562638. Accessed 9 Jun 2020

Dietterich HR, Diefenbach A, Soule A, Zoeller M, Patrick M, Major J, Lundgren P (this issue) Lava effusion rates and erupted volume during the 2018 Kīlauea lower East Rift Zone eruption.

Dixon J, Stolper E, Holloway J (1995) An experimental study of water and carbon dioxide solubilities in mid-ocean ridge basaltic liquids Part I: calibration and solubility models. J Petrol 36:1607–1631. https://doi.org/10.1093/oxfordjournals.petrology.a037267

DOH (2019) Hawai'i greenhouse gas emissions report for 2015, Hawai'i State Department of Health. https://health.hawaii.gov/cab/files/2019/02/2015-Inventory_Final-Report_January-2019-004-1.pdf. Accessed 25 Oct 2019.

Eguchi K, Uno I, Yumimoto K, Takemura T, Nakajima TY, Uematsu M, Liu Z (2011) Modulation of cloud droplets and radiation over the North Pacific by sulfate aerosol erupted from Mount Kīlauea. Scientific Online Letters on the Atmosphere 7:77–80. https://doi.org/10.2151/sola.2011-020

Elias T, Sutton AJ (2002) Sulfur dioxide emission rates from Kīlauea Volcano, Hawai'i, an update: 1998–2001. US Geological Survey Open-File Report 02–460, 29 pages. https://doi.org/10.3133/ofr2002460

Elias T, Sutton AJ (2007) Sulfur dioxide emission rates from Kīlauea Volcano, Hawai'i, an update: 2002–2006. US Geological Survey Open-File Report 2007–1114, 37 pages. https://pubs.usgs.gov/of/2007/1114/. Accessed 9 Jun 2020

Elias T, Sutton AJ (2012) Sulfur dioxide emission rates from Kīlauea Volcano, Hawai'i, 2007-2010. US Geological Survey Open-File Report 2012-1107, 26 pages. http://pubs.usgs.gov/of/2012/1107/. Accessed 9 Jun 2020

Elias T, Kern C, Horton KA, Sutton AJ, Garbeil H (2018) Measuring SO_2 emission rates at Kīlauea Volcano, Hawai'i, using an array of

upward-looking UV spectrometers, 2014–2017. Front Earth Sci 6:1–20. https://doi.org/10.3389/feart.2018.00214

Fickel M, Delgado Granados H (2017) On the use of different spectral windows in DOAS evaluations: effects on the estimation of SO_2 emission rate and mixing ratios during strong emission of Popocatépetl volcano. Chem Geol 462:67–73. https://doi.org/10.1016/j.chemgeo.2017.05.001

Fioletov VE, McLinden CA, Krotkov N, Li C, Joiner J, Theys N, Carn S, Moran MD (2016) A global catalogue of large SO_2 sources and emissions derived from the Ozone Monitoring Instrument. Atmos Chem Phys 16:11497–11519. https://doi.org/10.5194/acp-16-11497-2016

Fischer TP, Arellano S, Carn S, Aiuppa A, Galle B, Allard P, Lopez T, Shinohara H, Kelly P, Werner C, Cardellini C, Chiodini G (2019) The emissions of CO_2 and other volatiles from the world's subaerial volcanoes. Sci Rep 9:1–11. https://doi.org/10.1038/s41598-019-54682-1

Fortin MA, Riddle J, Desjardins-Langlais Y, Baker DR (2015) The effect of water on the sulfur concentration at sulfide saturation (SCSS) in natural melts. Geochim Cosmochim Acta 160:100–116. https://doi.org/10.1016/j.gca.2015.03.022

Frieß U, Monks PS, Remedios JJ, Rozanov A, Sinreich R, Wagner T, Platt U (2006) MAX-DOAS O4 measurements: a new technique to derive information on atmospheric aerosols: 2. Modeling studies J Geophys Res 111:D14203. https://doi.org/10.1029/2005JD006618

Galle B, Oppenheimer C, Geyer A, McGonigle AJS, Edmonds M, Horrocks L (2002) A miniaturised ultraviolet spectrometer for remote sensing of SO_2 fluxes: a new tool for volcano surveillance. J Volcanol Geotherm Res 119:241–254. https://doi.org/10.1016/S0377-0273(02)00356-6

Galle B, Johansson M, Rivera C, Zhang Y, Kihlman M, Kern C, Lehmann T, Platt U, Arellano S, Hidalgo S (2010) Network for Observation of Volcanic and Atmospheric Change (NOVAC)—a global network for volcanic gas monitoring: network layout and instrument description. J Geophys Res 115:D05304. https://doi.org/10.1029/2009JD011823

Gansecki C, Lee RL, Shea T, Lundblad SP, Hon K, Parcheta C (2019) The tangled tale of Kīlauea's 2018 eruption as told by geochemical monitoring. Science (80) 1212:1–9. https://doi.org/10.1126/science.aaz0147

Gatebe CK, Varnai T, Poudyal R, Ichoku C, King MD (2012) Taking the pulse of pyrocumulus clouds. Atmos Environ 52:121–130. https://doi.org/10.1016/j.atmosenv.2012.01.045

Gerlach TM (1986) Exsolution of H_2O, CO_2, and S during eruptive episodes at Kilauea Volcano, Hawaii. J Geophys Res 91:12177–12185. https://doi.org/10.1029/JB091iB12p12177

Gerlach TM (2004) Volcanic sources of tropospheric ozone-depleting trace gases. Geochem Geophys Geosyst 5:1–16. https://doi.org/10.1029/2004GC000747

Gerlach TM, McGee KA, Elias T, Sutton AJ, Doukas MP (2002) Carbon dioxide emission rate of Kilauea Volcano: implications for primary magma and the summit reservoir. J Geophys Res 107:ECV 3-1–ECV 3-15. https://doi.org/10.1029/2001JB000407

GHS/OCD (2018) Volcanic haze reaches the Marianas; those with respiratory issues advised to take precautions. Guam Homeland Security, Office of Civil Defense, https://www.ghs.guam.gov/volcanic-haze-reaches-marianas-those-respiratory-issues-advised-take-precautions. Accessed 11 Aug 2019.

Giambelluca TW, Chen Q, Frazier AG, Price JP, Chen YL, Chu PS, Eischeid JK, Delparte DM (2013) Online rainfall atlas of Hawai'i. Bull Am Meteorol Soc 94:313–316. https://doi.org/10.1175/BAMS-D-11-00228.1

Gíslason SR, Stefánsdóttir G, Pfeffer MA, Barsotti S, Jóhannsson T, Galeczka I, Bali E, Sigmarsson O, Stefánsson A, Keller NS, Sigurdsson Á, Bergsson B, Galle B, Jacobo VC, Arellano S, Aiuppa A, Jónasdóttir EB, Eiríksdóttir ES, Jakobsson S,

Guðfinnsson GH, Halldórsson SA, Gunnarsson H, Haddadi B, Jónsdóttir I, Thordarson T, Riishuus M, Högnadóttir T, Dürig T, Pedersen GBM, Höskuldsson Á, Gudmundsson MT (2015) Environmental pressure from the 2014-15 eruption of Barðarbunga volcano, Iceland. Geochemical Perspect Lett 1:84–93. https://doi.org/10.7185/geochemlet.1509

Grainger JF, Ring J (1962) Anomalous Fraunhofer line profiles. Nature 193:762. https://doi.org/10.1038/193762a0

Guo S, Bluth GJS, Rose WI, Watson IM, Prata AJ (2004) Re-evaluation of SO_2 release of the 15 June 1991 Pinatubo eruption using ultraviolet and infrared satellite sensors. Geochem Geophys Geosyst 5:1–31. https://doi.org/10.1029/2003GC000654

Gutmann A, Bobrowski N, Roberts TJ, Rüdiger J, Hoffmann T (2018) Advances in bromine speciation in volcanic plumes. Front Earth Sci 6. https://doi.org/10.3389/feart.2018.00213

Hastings WK (1970) Monte Carlo sampling methods using Markov chains and their applications. Biometrika 57:97–109. https://doi.org/10.1093/biomet/57.1.97

HDOH (2011) DOH guidance on short-term sulfur dioxide (SO_2) advisory levels. http://www.hiso2index.info/assets/FinalSO2Exposurelevels.pdf. Accessed 1 Sep 2019

Heliker C, Mattox TN (2003) The first two decades of the Puʻu ʻŌʻō-Kūpaianaha eruption: chronology and selected bibliography, in The Puʻu ʻŌʻō-Kūpaianaha eruption of Kilauea Volcano, Hawaii: the first 20 years, Heliker C, Swanson D, Takahashi T (eds) U.S. Geological Survey Professional Paper 1676, https://doi.org/10.3133/pp1676

Hermans C (2010) Measurement of absorption cross sections and spectroscopic molecular parameters - O_2 and its collisonal induced absorption. http://spectrolab.aeronomie.be/o2.htm. Accessed 20 Mar 2019

Holland L, Businger S, Elias T, Cherubini T (2020) Two ensemble approaches for forecasting sulfur dioxide emissions from Kīlauea Volcano. Weather Forecast, accepted for publication.

Houghton BF, Swanson DA, Carey RJ, Rausch J, Sutton AJ (2011) Pigeonholing pyroclasts: insights from the 19 March 2008 explosive eruption of Kīlauea Volcano. Geology 39:263–266. https://doi.org/10.1130/G31509.1

Hsieh PA, Ingebritsen SE (2019) Groundwater inflow toward a preheated volcanic conduit: application to the 2018 eruption at Kīlauea Volcano, Hawaiʻi. J Geophys Res Solid Earth, 124. https://doi.org/10.1029/2018jb017133

IPCC (2014) Climate change 2014: synthesis report. Contribution of working groups I, II and III to the fifth assessment report of the Intergovernmental Panel on Climate Change. 151p. ISBN 978-92-9169-143-2

James MR, Carr BB, D'Arcy F, Diefenbach AK, Dietterich HR, Fornaciai A, Lev E, Liu EJ, Pieri DC, Rodgers M, Smets B, Terada A et al (2020) Volcanological applications of unoccupied aircraft systems (UAS): developments, strategies, and future challenges. Volcanica 3:55–102. https://doi.org/10.30909/vol.03.01.67114

Johansson M, Galle B, Zhang Y, Rivera C, Chen D, Wyser K (2009) The dual-beam mini-DOAS technique—measurements of volcanic gas emission, plume height and plume speed with a single instrument. Bull Volcanol 71:747–751. https://doi.org/10.1007/s00445-008-0260-8

Kantzas EP, McGonigle AJS (2008) Ground based ultraviolet remote sensing of volcanic gas plumes. Sensors 8:1559–1574. https://doi.org/10.3390/s8031559

Kazahaya K, Shinohara H, Uto K, Odai M, Nakahori Y, Mori H, Iino H, Miyashita M, Hirabayashi J (2004) Gigantic SO_2 emission from Miyakejima volcano, Japan, caused by caldera collapse. Geology 32:425–428. https://doi.org/10.1130/G20399.1

Kelly P, Clor L, Diefenbach A, Lerner A, Elias T, Nadeau P, Werner C, Kern C et al. (this issue) Drone-borne monitoring of volcanic plume compositions during the 2018 rift eruption of Kīlauea Volcano.

Kern C, Deutschmann T, Vogel L, Wöhrbach M, Wagner T, Platt U (2010) Radiative transfer corrections for accurate spectroscopic measurements of volcanic gas emissions. Bull Volcanol 72:233–247. https://doi.org/10.1007/s00445-009-0313-7

Kern C, Deutschmann T, Werner C, Sutton AJ, Elias T, Kelly PJ (2012) Improving the accuracy of SO_2 column densities and emission rates obtained from upward-looking UV-spectroscopic measurements of volcanic plumes by taking realistic radiative transfer into account. J Geophys Res 117:D20302. https://doi.org/10.1029/2012JD017936

Kraus S (2004) DOASIS - DOAS Intelligent System. https://doasis.iup.uni-heidelberg.de/bugtracker/projects/doasis/download.php. Accessed 9 Jun 2020

Krotkov NA, Krueger AJ, Bhartia PK (1997) Ultraviolet optical model of volcanic clouds for remote sensing of ash and sulfur dioxide. J Geophys Res 102:21891–21904. https://doi.org/10.1029/97JD01690

Lerner A, Wallace P, Mourey A, deGraffenried R, Shea T, Lee R, Gansecki C, Nadeau P, Elias T, Kern C, Clor L, Kelly P, Werner C, Moore L (2019) Sulfur concentrations and oxidation states of products from the 2018 Kīlauea fissure eruption based on melt inclusions, embayments, and matrix glasses. AGU Fall Meeting Abstracts. https://agu.confex.com/agu/fm19/meetingapp.cgi/Paper/626603. Accessed 9 Jun 2020

Lerner A, Wallace P, Shea T, Morey A, Kelly P, Nadeau P, Elias T, Kern C, Clor L, Gansecki C, Lee R, Moore L, Werner C (this issue) The petrologic and degassing behavior of sulfur and magmatic volatiles from the 2018 eruption of Kīlauea Volcano, Hawaiʻi: melt concentrations, storage depths, and magma recycling.

Markov A (1906) Rasprostranenie zakona bol'shih chisel na velichiny, zavisyaschie drug ot druga. Izvestiya Fiziko-matematicheskogo obschestva pri Kazanskom universitete, 2-ya seriya 15(94):135–156

Mason E, Wieser P, Liu E, Ilyinskaya E, Edmonds M, Whitty RCW, Mather T, Elias T, Nadeau PA, Kern C, Schneider DJ (2020) Oppenheimer C (2020), Trace element emissions during the 2018 Kīlauea lower East Rift Zone eruption. EGU General Assembly. https://doi.org/10.5194/egusphere-egu2020-162

Mather TA, Pyle DM, Oppenheimer C (2003) Tropospheric volcanic aerosol. In: Robock A & Oppenheimer C. Volcanism and the Earth's atmosphere. Geophysical monograph series. American Geophysical Union, pp 189–212. https://doi.org/10.1029/13GM12

Mather TA, Witt MLI, Pyle DM, Quayle BM, Aiuppa A, Bagnato E, Martin RS, Sims KWW, Edmonds M, Sutton AJ, Ilyinskaya E (2012) Halogens and trace metal emissions from the ongoing 2008 summit eruption of Kīlauea Volcano, Hawaiʻi. Geochim Cosmochim Acta 83:292–323. https://doi.org/10.1016/j.gca.2011.11.029

Matsushima N (2005) H_2O emission rate by the volcanic plume during the 2000-2002 Miyakejima volcanic activity. Geophys Res Lett 32:L14307. https://doi.org/10.1029/2005GL023217

McCormick PM, Thomason LW, Trepte CR (1995) Atmospheric effects of the Mt Pinatubo eruption. Nature 373:399–404. https://doi.org/10.1038/373399a0

McGonigle AJS, Hilton DR, Fischer TP, Oppenheimer C (2005) Plume velocity determination for volcanic SO_2 flux measurements. Geophys Res Lett 32:11302. https://doi.org/10.1029/2005GL022470

Metropolis N, Rosenbluth AW, Rosenbluth MN, Teller AH, Teller E (1953) Equation of state calculations by fast computing machines. J Chem Phys 21:1087–1092. https://doi.org/10.1063/1.1699114

Mie G (1908) Beiträge zur Optik trüber Medien, speziell kolloidaler Metallösungen. Ann Phys 4:377–445. https://doi.org/10.1002/andp.19083300302

Mori T, Mori T, Kazahaya K, Ohwada M, Hirabayashi J, Yoshikawa S (2006) Effect of UV scattering on SO_2 emission rate measurements. Geophys Res Lett 33:1–5. https://doi.org/10.1029/2006GL026285

Mori T, Hashimoto T, Terada A, Yoshimoto M, Kazahaya R, Shinohara H, Tanaka R (2016) Volcanic plume measurements using a UAV for the 2014 Mt. Ontake eruption. Earth, Planets Sp 68:49. https://doi.org/10.1186/s40623-016-0418-0

Mosegaard K, Tarantola A (1995) Monte Carlo sampling of solutions to inverse problems. J Geophys Res 100:12,431–12,447. https://doi.org/10.1029/94jb03097

Moussallam Y, Edmonds M, Scaillet B, Peters N, Gennaro E, Sides I, Oppenheimer C (2016) The impact of degassing on the oxidation state of basaltic magmas: a case study of Kīlauea Volcano. Earth Planet Sci Lett 450:317–325. https://doi.org/10.1016/j.epsl.2016.06.031

Neal CA, Brantley SR, Antolik L, Babb J, Burgess M, Calles K, Cappos M, Chang JC, Conway S, Desmither L, Dotray P, Elias T et al (2019) The 2018 rift eruption and summit collapse of Kīlauea Volcano. Science (80) 363:367–374. https://doi.org/10.1126/science.aav7046

NIOSH (1978) Occupational health guideline for sulphur dioxide. https://www.cdc.gov/niosh/docs/81-123/pdfs/0575.pdf. Accessed 8 Jan 2020.

Oppenheimer C, Tsanev V, Braban C, Cox R, Adams J, Aiuppa A, Bobrowski N, Delmelle P, Barclay J, McGonigle A (2006) BrO formation in volcanic plumes. Geochim Cosmochim Acta 70:2935–2941. https://doi.org/10.1016/j.gca.2006.04.001

Orr TR, Poland MP, Patrick MR, Thelen WA, Sutton AJ, Elias T, Thornber CR, Parcheta C, Wooten KM (2015) Kīlauea's 5–9 March 2011 Kamoamoa fissure eruption and its relation to 30+ years of activity from Puʻu ʻŌʻō. In: Carey R, Cayol V, Poland M, Weis D (eds) Hawaiian volcanoes: from source to surface, Geophysical monograph series. John Wiley and Sons, Inc., pp 393–420. https://doi.org/10.1002/9781118872079.ch18

Patrick MR, Orr TR, Swanson DA, Elias T, Shiro B (2018) Lava lake activity at the summit of Kīlauea Volcano in 2016. US Geol Surv Sci Investig Rep 2018–5008:58. https://doi.org/10.3133/sir20185008

Patrick MR, Dietterich HR, Lyons JJ, Diefenbach AK, Parcheta C, Anderson KR, Namiki A, Sumita I, Shiro B, Kauahikaua JP (2019a) Cyclic lava effusion during the 2018 eruption of Kīlauea Volcano. Science 366:eaay9070, 1–10. https://doi.org/10.1126/science.aay9070

Patrick M, Orr T, Anderson K, Swanson D (2019b) Eruptions in sync: improved constraints on Kīlauea Volcano's hydraulic connection. Earth Planet Sci Lett 507:50–61. https://doi.org/10.1016/j.epsl.2018.11.030

Patrick MR, Houghton B, Poland MP, Anderson KR, Montgomery-Brown E, Johanson I, Thelen W, Elias T (2020) What caused the 2018 Kīlauea eruption? Cascading events and lessons for future forecasting. Nat Comm (in review)

Patrick M, Johanson I, Shea T, Waite G (this issue) The historic events at Kīlauea Volcano in 2018: summit collapse, rift zone eruption, and M_w 6.9 earthquake: preface to the special issue, Bull Volc 82:46, https://doi.org/10.1007/s00445-020-01377-5

Pfeffer MA, Bergsson B, Barsotti S, Stefánsdóttir G, Galle B, Arellano S, Conde V, Donovan A, Ilyinskaya E, Burton M, Aiuppa A, Whitty RCW, Simmons I, Arason Þ, Jónasdóttir E, Keller N, Yeo R, Arngrímsson H, Jóhannsson Þ, Butwin M, Askew R, Dumont S, von Löwis S, Ingvarsson Þ, la Spina A, Thomas H, Prata F, Grassa F, Giudice G, Stefánsson A, Marzano F, Montopoli M, Mereu L (2018) Ground-based measurements of the 2014-2015 Holuhraun volcanic cloud (Iceland). Geosci 8:1–25. https://doi.org/10.3390/geosciences8010029

Platt U, Stutz J (2008) Differential optical absorption spectroscopy - principles and applications. Springer, Berlin, Heidelberg. https://doi.org/10.1007/978-3-540-75776-4

Poulidis AP, Renfrew IA, Matthews AJ (2016) Thermally induced convective circulation and precipitation over an isolated volcano. J Atmos Sci 73:1667–1686. https://doi.org/10.1175/JAS-D-14-0327.1

Realmuto VJ, Elias T, Kern C, Krotkov NA, Li C (2018) Addressing the challenges of ground-based monitoring of SO_2 emissions from the lower East Rift Zone eruption of Kīlauea Volcano with satellite-based thermal infrared remote sensing. AGU Fall Meeting Abstracts. https://agu.confex.com/agu/fm18/meetingapp.cgi/Paper/455694. Accessed 9 Jun 2020

Roberts TJ (2018) Ozone depletion in tropospheric volcanic plumes: from halogen-poor to halogen-rich emissions. Geosciences 8:68. https://doi.org/10.3390/geosciences8020068

Roberts TJ, Vignelles D, Liuzzo M, Giudice G, Aiuppa A, Coltelli M, Salerno G, Chartier M, Couté B, Berthet G, Lurton T, Dulac F, Renard JB (2018) The primary volcanic aerosol emission from Mt Etna: size-resolved particles with SO_2 and role in plume reactive halogen chemistry. Geochim Cosmochim Acta 222:74–93. https://doi.org/10.1016/j.gca.2017.09.040

Rowe MC, Thornber CR, Orr TR (2015) Primitive components, crustal assimilation, and magmatic degassing during the early 2008 Kīlauea summit eruptive activity. In: Cayol V, Poland M, Weis D (eds) Carey R. Hawaiian Volcanoes, From Source to Surface. Geophysical monograph series, pp 439–455. https://doi.org/10.1002/9781118872079.ch20

Rüdiger J, Tirpitz JL, de Moor JM, Bobrowski N, Gutmann A, Liuzzo M, Ibarra M, Hoffmann T (2018) Implementation of electrochemical, optical and denuder-based sensors and sampling techniques on UAV for volcanic gas measurements: examples from Masaya, Turrialba and Stromboli volcanoes. Atmos Meas Tech 11:2441–2457. https://doi.org/10.5194/amt-11-2441-2018

Sawyer GM, Salerno GG, Le Blond JS, Martin RS, Spampinato L, Roberts TJ, Mather TA, Witt MLI, Tsanev VI, Oppenheimer C (2011) Gas and aerosol emissions from Villarrica volcano, Chile. J Volcanol Geotherm Res 203:62–75. https://doi.org/10.1016/j.jvolgeores.2011.04.003

Shinohara H, Fukui K, Kazahaya K, Saito G (2003) Degassing process of Miyakejima volcano: implications of gas emission rate and melt inclusion data. Dev Volcanol 5:147–161. https://doi.org/10.1016/S1871-644X(03)80028-1

Simmons IC, Pfeffer MA, Calder ES, Galle B, Arellano S, Coppola D, Barsotti S (2017) Extended SO_2 outgassing from the 2014–2015 Holuhraun lava flow field, Iceland. Bull Volcanol 79:1–11. https://doi.org/10.1007/s00445-017-1160-6

Soden BJ, Wetherald RT, Stenchikov GL, Robock A (2002) Global cooling after the eruption of Mount Pinatubo: a test of climate feedback by water vapor. Science 296:727–730. https://doi.org/10.1126/science.296.5568.727

Stearns HT (1925) The explosive phase of Kilauea Volcano, Hawaii, in 1924. Bull Volcanol 2:193–208. https://doi.org/10.1007/BF02719505

Stix J, de Moor JM, Rüdiger J, Alan A, Corrales E, D'Arcy F, Diaz JA, Liotta M (2018) Using drones and miniaturized instrumentation to study degassing at Turrialba and Masaya volcanoes, Central America. J Geophys Res Solid Earth 123:6501–6520. https://doi.org/10.1029/2018JB015655

Stutz J, Platt U (1996) Numerical analysis and estimation of the statistical error of differential optical absorption spectroscopy measurements with least-squares methods. Appl Opt 35:6041–6053. https://doi.org/10.1364/AO.35.006041

Sutton AJ, Elias T (2014) One hundred volatile years of volcanic gas studies at the Hawaiian volcano observatory. In: USGS Professional Paper 1801, characteristics of Hawaiian volcanoes, pp 295–320. https://doi.org/10.3133/pp1801

Sutton AJ, Elias T, Kauahikaua J (2003) Lava-effusion rates for the Puʻu ʻŌʻō -Kūpaianaha eruption derived from SO_2 emissions and very

low frequency (VLF) measurements. In: Heliker C, Swanson D, Takahashi T (eds) The Puʻu ʻŌʻō -Kūpaianaha eruption of Kīlauea Volcano, Hawaiʻi: the first 20 years. U.S. Geological Survey, Reston, pp 137–148. https://doi.org/10.3133/pp1676

Swanson D, Wooten K, Orr T (2009) Buckets of ash track tephra flux from Halemaʻumaʻu Crater, Hawaiʻi. Eos 90:427–428. https://doi.org/10.1029/2008eo220003

Symonds RB, Gerlach TM, Reed MH (2001) Magmatic gas scrubbing: implications for volcano monitoring. J Volcanol Geotherm Res 108: 303–341. https://doi.org/10.1016/S0377-0273(00)00292-4

Tam E, Miike R, Labrenz S, Sutton AJ, Elias T, Davis J, Chen Y-L, Tantisira K, Dockery D, Avol E (2016) Volcanic air pollution over the Island of Hawaiʻi: emissions, dispersal, and composition. Association with respiratory symptoms and lung function in Hawaiʻi Island school children. Environ Int 92–93:543–552. https://doi.org/10.1016/j.envint.2016.03.025

Tang Y, Tong DQ, Yang K, Lee P, Baker B, Crawford A, Luke W, Stein A, Campbell PC, Ring A, Flynn J, Wang Y, McQueen J, Pan L, Huang J, Stajner I (2020) Air quality impacts of the 2018 Mt. Kilauea Volcano eruption in Hawaii: A regional chemical transport model study with satellite-constrained emissions. Atmos Environ. https://doi.org/10.1016/j.atmosenv.2020.117648

Textor C, Graf H-F, Timmreck C, Robock A (2004) Emissions from volcanoes. In: Granier C, Artaxo P, Reeves C (eds) Emissions of atmospheric trace compounds. Springer, Berlin, Heidelberg, pp 269–303 https://doi.org/10.1007/978-1-4020-2167-1_7

Theys N, Hedelt P, De Smedt I, Lerot C, Yu H, Vlietinck J, Pedergnana M, Arellano S, Galle B, Fernandez D, Barrington C, Taisne B et al (2019) Global monitoring of volcanic SO_2 degassing from space with unprecedented resolution. Sci Rep 9:1–10. https://doi.org/10.1038/s41598-019-39279-y

Thornber CR, Orr TR, Heliker C, Hoblitt RP (2015) Petrologic testament to changes in shallow magma storage and transport during 30+ years of recharge and eruption at Kīlauea Volcano, Hawaiʻi. In: Carey R, Cayol V, Poland M, Weis D (eds) Hawaiian volcanoes: from source to surface. Geophysical monograph series, pp 147–188. https://doi.org/10.1002/9781118872079.ch8

U.S. Environmental Protection Agency (EPA) (2019) Air emissions inventories. Air pollutant emissions trends data. Table national annual emissions trend. https://www.epa.gov/air-emissions-inventories/air-pollutant-emissions-trends-data. Accessed 24 Oct 2019.

U.S. Geological Survey (2018) Colorful plumes - can we see volcanic gases? USGS Volcano Watch, released 17 June 2018. https://www.usgs.gov/center-news/volcano-watch-colorful-plumes-can-we-see-volcanic-gases. Accessed 9 Jun 2020

Uno I, Eguchi K, Yumimoto K (2014) Eruption of Mt. Kilauea impacted cloud droplet and radiation budget over North Pacific. In: Uematsu M, Yokouchi Y, Watanabe YW, et al. (eds) Western Pacific air-sea interaction study. pp 83–87. https://doi.org/10.5047/w-pass.a01.009

Vandaele AC, Hermans C, Fally S (2009) Fourier transform measurements of SO_2 absorption cross sections: II. Temperature dependence in the 29 000-44 000 cm-1 (227-345 nm) region. J Quant Spectrosc Radiat Transf 110:2115–2126. https://doi.org/10.1016/j.jqsrt.2009.05.006

Vernier J-P, Kalnajs L, Diaz JA, Reese T, Corrales E, Alan A, Vernier H, Holland L, Patel A, Rastogi N, Wienhold F, Carn S, Krotkov N, Murray J (2020) VolKilau: volcano rapid response balloon campaign during the 2018 Kilauea eruption. Bull Am Meteorol Soc 1–40. https://doi.org/10.1175/bams-d-19-0011.1

von Glasow R, Bobrowski N, Kern C (2009) The effects of volcanic eruptions on atmospheric chemistry. Chem Geol 263:131–142. https://doi.org/10.1016/j.chemgeo.2008.08.020

Wagner T, Dix B, Friedeburg CV, Frieß U, Sanghavi S, Sinreich R, Platt U (2004) MAX-DOAS O_4 measurements: a new technique to derive information on atmospheric aerosols - principles and information content. J Geophys Res 109:1–19. https://doi.org/10.1029/2004JD004904

Werner C, Fischer T, Aiuppa A, Edmonds M, Cardellini C, Carn S, Chiodini G, Cottrrell E, Burton M, Shinohara H, Allard P (2019) Carbon dioxide emissions from subaerial volcanic regions - two decades in review. In: Orcutt BN, Daniel I, Dasgupta R (eds) Deep carbon - past to present. Cambridge University Press, pp 188–236. https://doi.org/10.1017/9781108677950

Whitty R, Ilyinskaya E, Mason E, Wieser P, Liu E, Edmonds M, Mather T, Elias T, Nadeau P, Kern C, Schneider D, Oppenheimer C (2019) Particle size and concentrations of volcanic aerosols of the 2018 Kīlauea lower East Rift Zone eruption. EGU General Assembly 2019. https://meetingorganizer.copernicus.org/EGU2019/EGU2019-495-1.pdf. Accessed 9 Jun 2020

Whitty RCW, Ilyinskaya E, Mason E, Wieser PE, Liu EJ, Schmidt A, Roberts T, Pfeffer MA, Brooks B, Mather TA, Edmonds M, Elias T, Schneider DJ, Oppenheimer C, Dybwad A, Nadeau PA, Kern C, (2020) Spatial and temporal variations in SO_2 and $PM_{2.5}$ levels around Kīlauea Volcano, Hawaiʻi during 2007–2018. Frontiers in Earth Science 8:36. https://doi.org/10.3389/feart.2020.00036

Wieser PE, Jenner FE, Edmonds M, Maclennan J, Kunz BE (2020) Chalcophile elements track sulfide saturation, sulfide resorption and magmatic degassing at Kīlauea Volcano, Hawaiʻi. Geochim Cosmochim Acta. https://doi.org/10.1016/j.gca.2020.05.018

Wood K, Albadra A, Berthoud L, Calway A, Watson M, Thomas H, Richardson T, Liu E, Chigna G (2019) Determining the three-dimensional structure of a volcanic plume using Unoccupied Aerial System (UAS) imagery. J Volcanol Geotherm Res, 106731. https://doi.org/10.1016/j.jvolgeores.2019.106731

Zhang S, Wu J, Fan W, Yang Q, Zhao D (2020) Review of aerosol optical depth retrieval using visibility data. Earth-Science Rev 200:102986. https://doi.org/10.1016/j.earscirev.2019.102986